ORIGINAL ARTICLE

Simulation of MJO with improved deep convection scheme in different resolutions of BCC-CSM2 models

Mengzhe Zheng[1,2] · Tongwen Wu[1,2,3] · Xiaoge Xin[2,3] · Xiangwen Liu[2,3] · Yixiong Lu[2,3] · Weihua Jie[2,3] · Chengjun Xie[1,4] · Yumeng Zhou[1,2]

Abstract

This study investigates the impacts of modifying the deep convection scheme on the ability to simulate the Madden–Julian Oscillation (MJO) in the Beijing Climate Center Climate System Model version 2 with a medium resolution (BCC-CSM2-T159) and a high resolution (BCC-CSM2-T382). On the basis of the original deep convection scheme, a modified scheme is suggested, which involves the transport processes of deep convective cloud water. The liquid cloud water that is detrained is transferred horizontally to its neighboring grids, and a portion of the cloud water that is horizontally transported is allowed to be transported downward into the lower troposphere. Both BCC-CSM2-T159 and BCC-CSM2-T382 with the modified deep convection scheme perform better than that used the original deep convection scheme in reproducing the major features of the MJO, such as its spectrum, period, intensity, eastward propagation and life cycle. Further analysis shows that those pronounced improvements in the MJO features in both BCC-CSM2-T159 and BCC-CSM2-T382 with the modified scheme are caused by transport processes of deep convective cloud water. The modified deep convection scheme enhances moisture and energy exchange from the lower troposphere to the upper troposphere around convective cloud, and promotes the convergence of moisture in the lower troposphere to the east of the MJO convection center, and then induces eastward propagation of the MJO. The comparisons between the coupled experiments and their corresponding experiments following Atmospheric Model Intercomparison Project (AMIP) simulations indicated that atmosphere–ocean interactions are also important to improve MJO simulations in the models.

Keywords MJO · MJO simulation · Deep convection scheme · Improvement · BCC-CSM2

1 Introduction

The Madden–Julian oscillation (MJO) is a widely recognized phenomenon with major contributions to the intraseasonal variability in the tropics (Madden and Julian 1971, 1972; Zhang 2005). The MJO has a broad impact on many weather and climate phenomena. The monsoon circulation, surface temperature, heavy precipitation in tropical areas, and weather and climate in mid- to high-latitudes are all influenced by MJO events (Wheeler et al. 2009; Lau and Waliser 2011; Zhang 2013; Zaitchik 2017; Zheng et al. 2018; Lenka et al. 2023; Wang et al. 2023). Extreme weather events have also been found to be connected with the MJO (Wheeler et al. 2009; Zhang 2013; Roxy et al. 2019; Miller et al. 2022). For example, Roxy et al. (2019) suggested that synergistic effects of the changes in the Indo-Pacific warm pool and the MJO in the context of global warming may trigger or exacerbate severe weather events such as floods and droughts. The probability of tornadoes and severe hail in the United States significantly increases during strong MJO events (Baggett et al. 2018; Miller et al. 2022). The generation, intensification and tracks of tropical cyclones are modulated by the MJO (Vitart 2009; Vitart and Molteni

✉ Tongwen Wu
  twwu@cma.gov.cn

✉ Xiaoge Xin
  xinxg@cma.gov.cn

1 Chinese Academy of Meteorological Sciences, China Meteorological Administration, Beijing 100081, China

2 Earth System Modeling and Prediction Centre, China Meteorological Administration, Beijing 100081, China

3 State Key Laboratory of Severe Weather, Chinese Academy of Meteorological Sciences, Beijing 100081, China

4 University of Chinese Academy of Sciences, Beijing 100049, China

2010; Klotzbach and Oliver 2015; Akhila et al. 2022; Klotzbach et al. 2023). Klotzbach and Oliver (2015) showed that tropical cyclones are more likely to be generated during the active phases of the MJO. Recent studies (e.g., Liang and Fedorov 2021; Feng et al. 2023; Latos et al. 2023) also suggested that the interaction of equatorial waves associated with the MJO provides a supportive environment for the occurrence and enhancement of tropical cyclone activity. MJO events with embedded tropical cyclones are the most important mechanism for generating westerly wind bursts (WWBs) and influence the occurrence and development of El Niño events (Liang and Fedorov 2021). The primary source of predictability for the sub-seasonal time scale also comes from the MJO (Lau and Waliser 2011; Li et al. 2015; Vitart et al. 2017).

Current climate models have the ability to simulate the basic features of the MJO. However, the majority of climate models still struggle to realistically reproduce the MJO (Jiang et al. 2015; Ahn et al. 2017; Wang and Lee 2017; Li et al. 2020). In the first Atmospheric Model Intercomparison Project (AMIP I), Slingo et al. (1996) showed that none of the 15 atmospheric general circulation models succeeded in reproducing the dominant intraseasonal oscillation. Lin et al. (2006) evaluated the MJO simulation ability of 14 coupled general circulation models (GCMs) participating in Phase 3 of the Coupled Model Intercomparison Project (CMIP3, Meehl et al. 2007), and indicated that 12 models underestimated the MJO variance and most lacked high coherence in the eastward propagation of the MJO. Jiang et al. (2015) evaluated MJO simulations of 27 GCMs participating in the Working Group on Numerical Experimentation MJO Task Force (MJOTF)/GEWEX Atmospheric System Study (GASS) MJO global model comparison project, and only eight models were able to simulate the systematic eastward propagation of the MJO and the baroclinic structure in the vertical u-wind. Compared to the CMIP3 models, most CMIP5 models showed a slight improvement in the simulation of the MJO (Taylor et al. 2012; Hung et al. 2013; Ahn et al. 2017). In the recent Phase 6 of the Coupled Model Intercomparison Project (CMIP6, Eyring et al. 2016), most of the models demonstrated significant improvements in the eastward propagation of the MJO, including more realistic propagation speeds and larger propagation distances (Li et al. 2022). However, it is still difficult to realistically simulate other features of the MJO, such as MJO amplitude, variance and period (Chen et al. 2022).

The simulation ability of the MJO in climate models is affected by a variety of factors, including the model resolution (e.g., Jia et al. 2008; Savarin and Chen 2022), model background mean state (Sperber et al. 2005; Ahn et al. 2019), atmosphere–ocean interactions (Pegion and Kirtman 2008; Newman et al. 2009; Chen and Zhang 2019; Zhao and Nasuno 2020), vertical heating profile (Cao and Zhang 2017;

Bartana et al.2023), and cumulus convection parameterization schemes (Del Genio et al. 2015; Kim and Maloney 2017; Liu et al. 2019). In particular, many studies have indicated a model's ability to reproduce the MJO is strongly dependent on the cumulus convection parameterization schemes used in the model (e.g., Duvel et al. 2013; Ling and Li 2014). Many attempts have been made to improve MJO simulation in climate models by improving a few specific aspects of the cumulus convective parameterization schemes. One aspect is that MJO simulation can be successfully improved by modifying the cumulus entrainment and detrainment rates in GCMs. Tokioka et al. (1988) added range limits of the cumulus entrainment rate of ambient air in the model and improved the simulation ability of intraseasonal oscillations in the tropics. Maloney and Hartmann (2001) improved the model's ability to simulate the MJO by optimizing the parameterization of convective precipitation evaporation in an unsaturated ambient and unsaturated downdraft. Ahn et al. (2019) suggested that GCMs using an adaptive entrainment rate could realistically simulate the mean state and MJO. Convective closure condition is also an important factor affecting MJO simulations. Previous studies have shown that modifying convection closure assumptions or adding a moisture/convection trigger condition to the convective scheme could also improve the simulation ability of tropical intraseasonal oscillations (Wang and Schlesinger 1999; Zhang and Mu 2005; Lin et al. 2008). Deng and Wu (2010) modified the convective momentum transport (CMT) in the deep convection scheme, resulting in significant improvements in both the signal and propagation of the MJO. Enhancing moisture-convection feedback in the model improves MJO simulations (Bechtold et al. 2008; Hannah and Maloney 2011; Liu et al. 2022). On the other hand, incorporating mesoscale stratiform heating structures by altering vertical heating structures in climate models could also significantly improve MJO simulations (e.g., Seo and Wang 2010; Cao and Zhang 2017). In addition to traditional convective parameterization, superparameterization (e.g., Khairoutdinov et al. 2005; Hannah et al. 2015) and stochastic parameterization (e.g., Deng et al. 2015; Goswami et al. 2017; Pathak et al. 2021) have been implemented to improve MJO simulations and predictions.

Air–sea interaction is also an important aspect affecting MJO simulations. Some studies showed that most GCMs could improve MJO simulations by introducing complete air–sea coupling. Tseng et al. (2022) found that the intensity, period, and propagation speed of the MJO were improved by coupling a one-column ocean model in the atmospheric general circulation model (AGCM). Introducing high-frequency air–sea coupling on a sub-daily scale could enhance the simulation of the MJO (Chen and Zhang 2019; Zhao and Nasuno 2020). However, there are a few GCMs in which air–sea interactions have little or even negative effects on the MJO simulations (e.g., Pegion and Kirtman 2008; Newman et al. 2009).

The Beijing Climate Center Climate System Model (BCC-CSM) is a completely coupled climate model developed by the China Meteorological Administration that includes atmosphere, land surface, ocean, and sea–ice components (Wu et al. 2013, 2014, 2019, 2021; Xin et al. 2013). Its first-generation models (BCC-CSM1.1 and BCC-CSM1.1 m) and second-generation models (BCC-CSM2-MR and BCC-CSM2-HR) with different resolutions participated in CMIP5 and CMIP6, respectively. BCC-CSM1.1 m has some deficiencies in simulating some basic features of the MJO, including the spectral distribution, intensity, structure, and propagation (Liu et al. 2019). In medium resolution version of BCC-CSM2-MR, the simulation ability in the main features of the MJO is improved in contrast to its previous version of BCC-CSM1.1 m with the same resolution, but the intensity is still weaker than the observations (Wu et al. 2019). Some new developments have been implemented in the high-resolution model BCC-CSM2-HR (Wu et al. 2021), in particular, the deep cumulus convection scheme first proposed by Wu (2012) has been further improved to allow the transport of detrained cloud water to neighboring grids and downward into the lower troposphere. The simulation of the MJO in BCC-CSM2-HR has evident improvements. Some features of the MJO can be accurately simulated by the model, including the behavior of eastward propagation and the propagation speed of the MJO (Wu et al. 2021). Wu et al. (2021) showed that BCC-CSM2-HR could realistically reproduce the main patterns of the atmosphere temperature and wind, precipitation, land surface air temperature and sea surface temperature (SST).

The purpose of this work is focused on the effects of the modified deep convection parameterization scheme used in BCC-CSM2-HR (Wu et al. 2021) on MJO simulations, in contrast to the previous deep convection scheme (Wu et al. 2012) in the two newly developed versions of BCC-CSM2. The impacts of sea–air interactions on MJO simulations using the corresponding atmospheric component models are also investigated in this study. The rest of this study is organized as follows. Section 2 describes the models, experimental design and data used in this study. Section 3 examines basic features of the mean state simulated by the models and explore the impact of the modified deep convection scheme on the simulation ability of the MJO. Section 4 includes summary and discussion.

2 Models, experimental design, and data used

2.1 Models

The models used in this study are the two newly-developed versions of the Beijing Climate Center (BCC) climate system model BCC-CSM2-T159 with a medium resolution of T159 ($0.75° \times 0.75°$) and BCC-CSM2-T382 with a high resolution of T382 ($0.3125° \times 0.3125°$) and 70 layers, with the top layer at 0.01 hPa in the atmosphere, respectively. They are developed on the basis of BCC-CSM2-HR (Wu et al. 2021). In BCC-CSM2-T159 and BCC-CSM2-T382, the corresponding atmospheric components are BCC-AGCM3 with T159 and T382 resolutions (hereafter referred to as BCC-AGCM3-T159 and BCC-AGCM3-T382), respectively.

The deep cumulus convection scheme used in BCC-CSM2-HR participated in CMIP6 (Wu et al. 2019) is the modified scheme based on the deep cumulus convection scheme suggested by Wu (2012). The original deep convection scheme disregards the effects of the convective updraft occurring in the same grid column on neighboring grids. With increased horizontal resolution of BCC-CSM, the effects of the deep convection process on the atmosphere in adjacent grids are not negligible. Some modifications are made based on the original deep convection scheme as follows:

(1) After convection initiation, the liquid cloud water in the rising cloud mass is generally detrained outside the grid box and transported horizontally to adjacent grids by atmospheric circulation. This process is conducted in the dynamical core.

(2) Part of the liquid cloud water transported to adjacent grids is assumed to downdraft into the lower troposphere. Atmospheric moisture and temperature will change accompanied with this downward transport process. The downward transport of moisture, denoted as $\left(\frac{\partial q}{\partial t}\right)_{downdraft}$, depends on the increase of the horizontally transferred liquid cloud water with time ($\Delta q_{dyn,adv}$), i.e.

$$\left(\frac{\partial q}{\partial t}\right)_{downdraft} = \Delta q_{dyn,adv} \cdot \varepsilon \cdot \Delta t \tag{1}$$

where ε is a constant and represents the intensity of the downward transport, and Δt is the dynamical time step. The Eq. (1) can be rewritten as

$$\left(\frac{\partial q}{\partial t}\right)_{downdraft} = \frac{\partial}{\partial z}(M \cdot q) \tag{2}$$

In which, M is the mass flux transported downward in neighboring grids and can be derived using the Eqs. (1) and (2). Here, the evaporation of liquid cloud water in the downward transport process is not considered. The evaporation or condensation for the additional part of water vapor transported by downward transport processes is treated by nonconvective cloud processes. The variation of atmospheric temperature accompanying the downward transport process can be derived using the Eq. (3).

$$\left(\frac{\partial T}{\partial t}\right)_{downdraft} = \frac{\partial}{\partial z}(M \cdot T) \tag{3}$$

2.2 Experimental design and data used

To investigate the effects of the improved deep convection scheme on MJO simulations, a set of contrast experiments are conducted for 10 years (1989–1998) using BCC-CSM2-T159 and BCC-CSM2-T382, respectively. In the experiments with the modified scheme (MS) and the original scheme (OS), we use the same initial data from historical experiments participating in CMIP6. The realistic external forcing data include solar constants, aerosols, greenhouse gases, ozone, volcanoes, and land use, which are the same as those used in the CMIP6 historical simulations (Wu et al. 2019). In addition, the AMIP-like experiments are conducted for the same decade using BCC-AGCM3-T159 and BCC-AGCM3-T152, in which the 1989–1998 monthly observed sea surface temperature (SST) and sea ice temperature are used and downloaded from https://www.metoffice.gov.uk/hadobs/en4. Moreover, the other external forcing data are the same as those used in the coupled models.

The observed precipitation with a horizontal resolution of $1.0° \times 1.0°$ is obtained from the Global Precipitation Climatology Project Version 1.3 dataset (GPCP, Adler et al. 2017). Daily observed global outgoing longwave radiation (OLR) is from the National Oceanic and Atmospheric Administration (NOAA) with a resolution of $2.5° \times 2.5°$ (Liebmann and Smith 1996). The fifth generation ECMWF reanalysis (ERA5) data with a resolution of $0.25° \times 0.25°$ are used to verify the simulated atmospheric circulation, SST and specific humidity (Hersbach et al. 2018).

In the evaluation, the model output, GPCP precipitation and ERA5 data are all interpolated onto a $2.5° \times 2.5°$ horizontal grid to match the observed OLR data. For the analysis in Sect. 3.5, the simulated precipitation, moisture and wind fields are not interpolated to preserve the original information of the model output. In the analysis, we focus on the anomaly fields of the variables, which are extracted by removing the annual average of the original daily data. The 20–100 days Lanczos bandpass filter is used to obtain the intraseasonal information. The principal components of the MJO are obtained by performing multivariate Combined Empirical Orthogonal Function expansion (CEOF) of intraseasonal outgoing longwave radiation (OLR), 850-hPa zonal wind (U850), and 200-hPa zonal wind (U200). The evaluation of the MJO focuses on the boreal winter (November to April) in the tropics (10° S–10° N).

3 Results

3.1 Basic features of the climatological mean state

The ability of a climate model to reproduce the distribution of the climatological mean precipitation is the basis for

accurate simulation of the MJO. As shown in Fig. 1, the OS and MS experiments of BCC-CSM2-T159 and BCC-CSM2-T382 can all reproduce the basic geographic distribution of precipitation in the boreal winter with pattern correlation coefficient (PCC) above 0.88, although the experiments all overestimate the precipitation in the equatorial convergence zone. There is little difference between the PCCs of the OS and MS experiments for each model. The OS and MS experiments differ in the intensity of winter precipitation in the tropical convergence zone, which is more evident in the high-resolution model (BCC-CSM2-T382). In BCC-CSM2-T382, the precipitation intensity in the tropical Pacific simulated by the MS experiment is closer to the observations than the OS experiment. In addition, BCC-CSM2-T382 shows a better ability to simulate the zonal precipitation band at 0–10° N in the equatorial Pacific than both the OS and MS experiments of BCC-CSM2-T159, indicating the better performance of the high-resolution version of BCC-CSM2 in the intertropical convergence zone.

In the boreal summer, distributions of precipitation are similar between the OS and MS experiments of each model with approximate PCCs (Fig. 2). BCC-CSM2-T382 performs better in reproducing summer precipitation than BCC-CSM2-T159, with higher spatial correlation coefficients in both the OS and MS experiments of BCC-CSM2-T382. Compared to BCC-CSM2-T159, BCC-CSM2-T382 has an obvious improvement in the intensity of precipitation in the South Pacific convergence zone in the boreal summer.

The improved deep convection scheme does not cause evident variations in the amount of convective rainfall. Figure 3 shows the annual mean state of convective precipitation over the tropics for the OS experiments in BCC-CSM2-T159 and BCC-CSM2-T382 and the differences between the corresponding MS and OS experiments. Convective precipitation for the OS experiments in both BCC-CSM2-T159 and BCC-CSM2-T382 is concentrated in the Intertropical Convergence Zone (Fig. 3a, c). There are no significant systematic differences between the MS and OS experiments of either both BCC-CSM2-T159 or BCC-CSM2-T382 (Fig. 3b, d). Compared to the OS experiments, the MS experiments in BCC-CSM2-T159 and BCC-CSM2-T382 simulate a little increase of convective precipitation on maritime continents and a small decrease over the western equatorial Pacific. Compared to BCC-CSM2-T159, the high-resolution version BCC-CSM2-T382 simulates less convective precipitation over the equatorial Indo-Pacific regions.

The sea surface temperature mean state is also an important factor influencing MJO simulations (Landu and Maloney 2011). The annual mean state of the observed SST over the tropics and the biases between the simulations and observations are shown in Fig. 4. The OS and MS experiments of both BCC-CSM2-T159 and BCC-CSM2-T382 simulate almost identical spatial distributions of SST biases
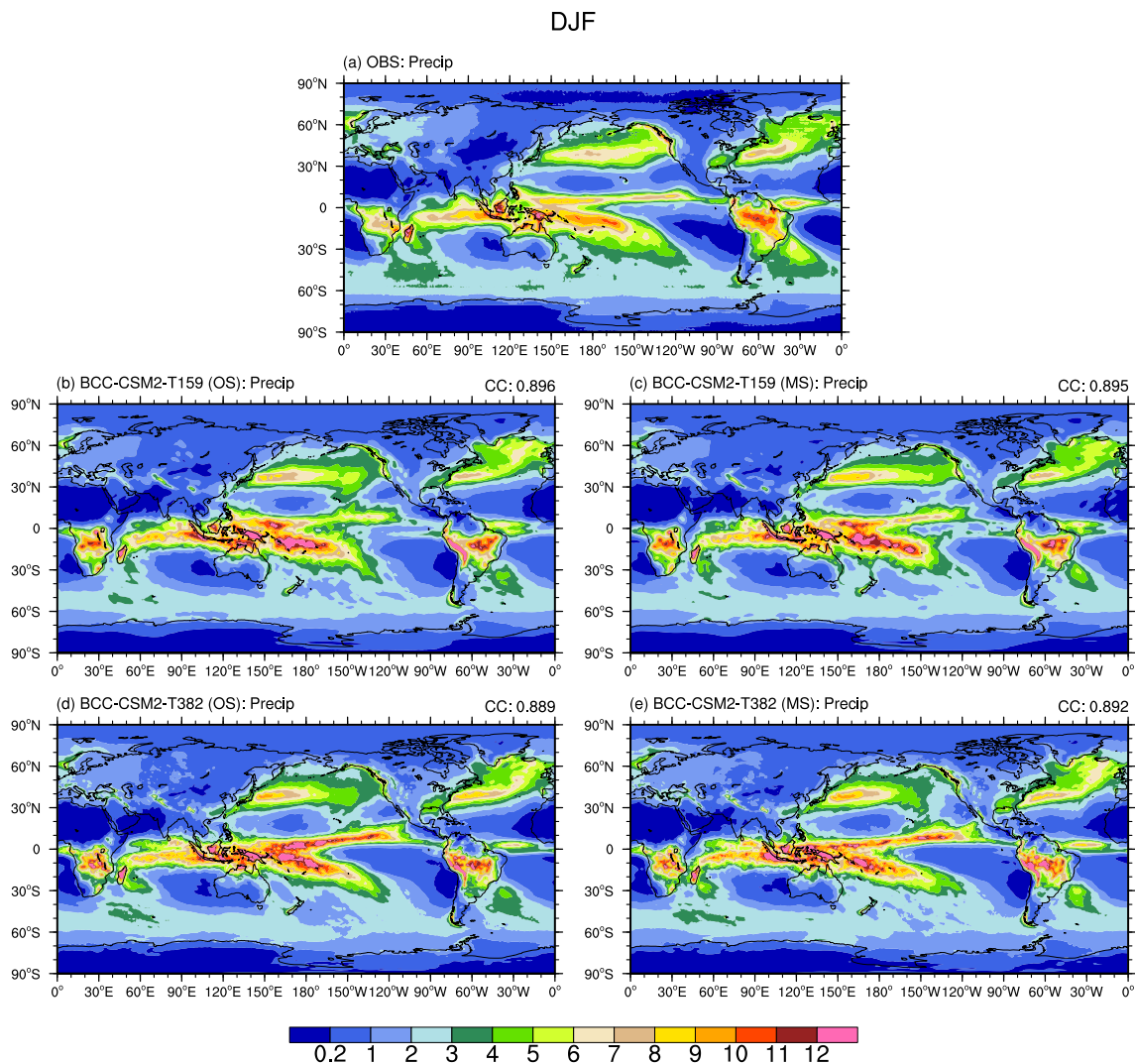
DJF

Fig. 1 Climatological mean boreal winter (December–January–February) precipitation (unit: mm day^{-1}) for **a** GPCP, **b** BCC-CSM2-T159 (OS), **c** BCC-CSM2-T159 (MS), **d** BCC-CSM2-T382 (OS), and **e** BCC-CSM2-T382 (MS) from 1989 to 1998. The number in the top right of the panel is the spatial correlation coefficient between the observations and simulations

in contrast to the observed climatology. The OS and MS experiments in BCC-CSM2-T159 show warm biases of the SST about ~1 °C near the maritime continents (Fig. 4b, c), and weak cold biases in the central to eastern equatorial Pacific (Fig. 4d, e). These biases along the equatorial Pacific are slightly enhanced in the high-resolution version BCC-CSM2-T382. The similar biases in OS and MS experiments for both BCC-CSM2-T159 and BCC-CSM2-T382 indicate that the improved deep convection scheme does not lead to evident variations in the SST climatology.

The globally averaged shortwave radiative forcing of the MS experiment in BCC-CSM2-T159 is -50.4 W m^{-2}, which is slightly stronger than that of the OS experiment, at -50.1 W m^{-2}, and both are within the range of the CERES-EBAF observations (− 47.5 ± 3 W m^{-2}) (Stephens et al. 2012; Wild

2020). The high-resolution version BCC-CSM2-T382 shows a smaller difference between MS and OS experiments of − 49.5 W m^{-2} and − 49.3 W m^{-2}, respectively. The globally-averaged longwave cloud radiative forcing for the MS and OS experiments in BCC-CSM2-T159 is 30.4 W m^{-2} and 30.3 W m^{-2}, respectively, which is within the observational uncertainty range (± 3 W m^{-2}) of the CERES reference value (28 W m^{-2}). The globally-averaged longwave radiative forcing simulated by the MS and OS experiments in BCC-CSM2-T382 is closer to the reference value than BCC-CSM2-T159, at 27.9 W m^{-2} and 28.1 W m^{-2}, respectively. The simulations of cloud radiative forcing in BCC-CSM2-T159 and BCC-CSM2-T382 are within reasonable ranges for both OS and MS experiments and the improved deep convection scheme has less impact on cloud radiative forcing.
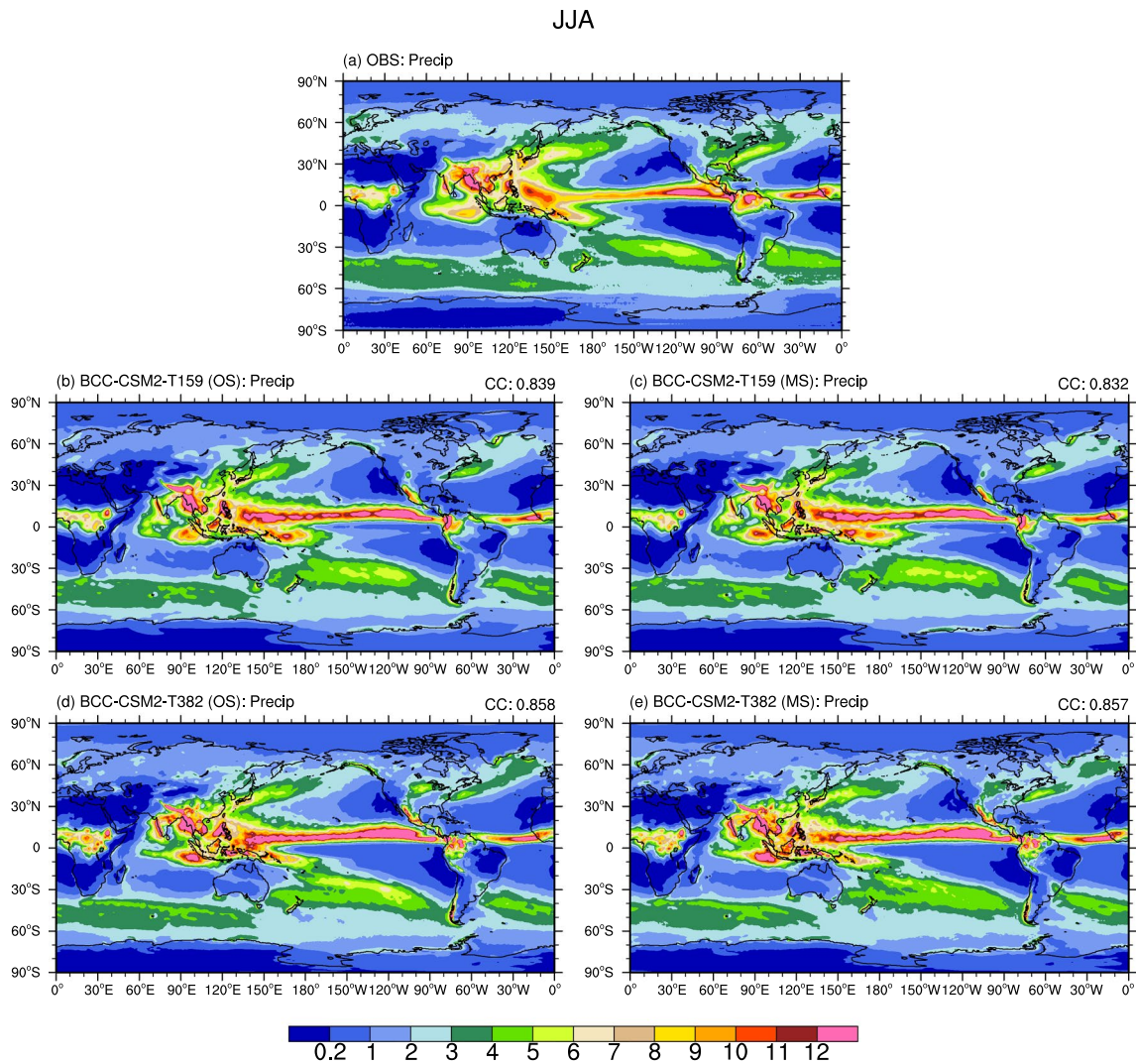
JJA

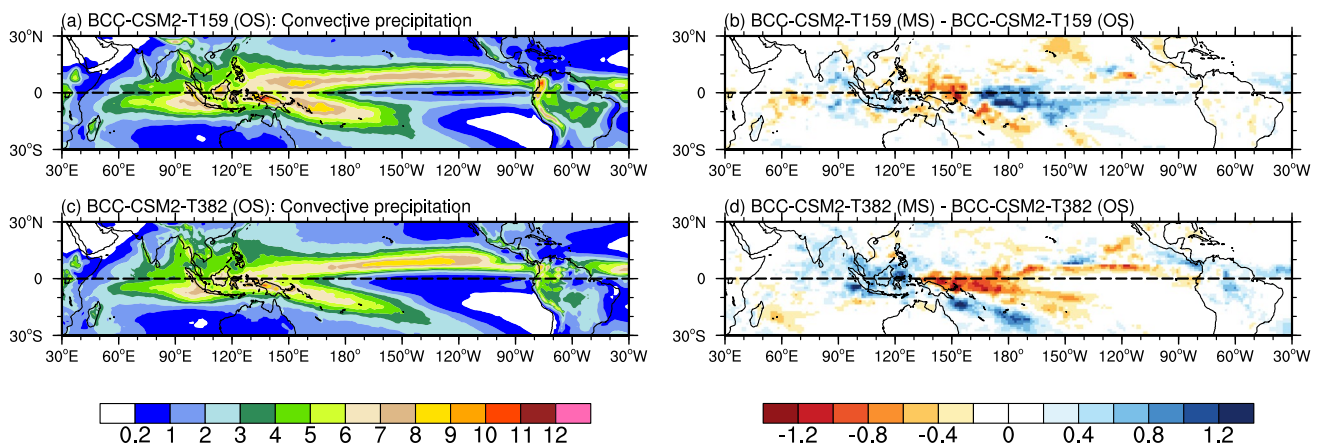**Fig. 2** The same as Fig. 1 but for the boreal summer (June–July–August)

Fig. 3 Annual mean convective precipitation (unit: mm day.$^{-1}$) from **a** BCC-CSM2-T159 (OS) and **c** BCC-CSM2-T382 (OS) experiments, and **b**, **d** the differences between the MS and OS experiments of BCC-CSM2-T159 and BCC-CSM2-T382
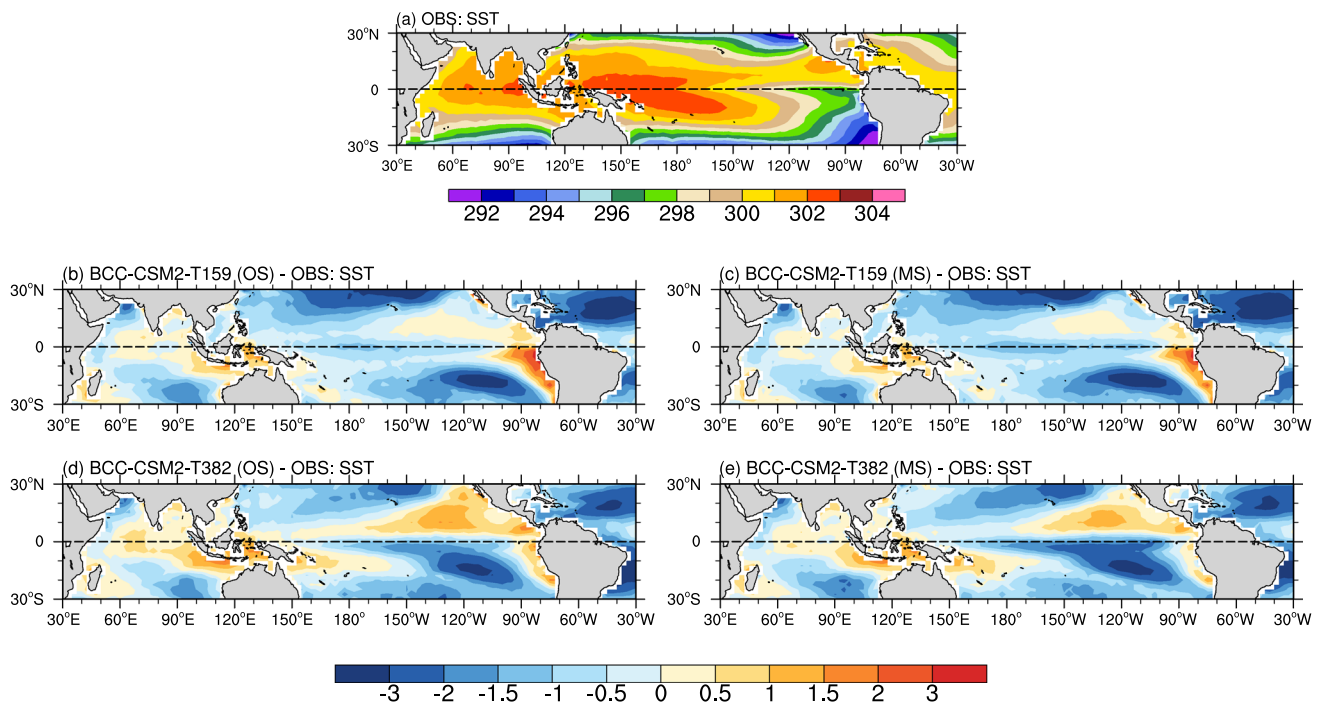
Fig. 4 Annual mean state of sea surface temperature (unit: K) for **a** ERA5 SST observations and the model biases of **b** BCC-CSM2-T159 (OS), **c** BCC-CSM2-T159 (MS), **d** BCC-CSM2-T382 (OS), and **e** BCC-CSM2-T382 (MS) in contrast to ERA5 SST from 1989 to 1998

3.2 MJO basic features

In this section, the MJO simulation diagnostics generated by the US Climate Variability and Predictability MJO Working Group (MJOWG, Waliser et al. 2009) are applied to the BCC models to assess the model's ability to simulate basic features of the MJO. We also calculate MJO skill metrics to quantitatively assess and diagnose the performance of the models in simulating MJO features (Ahn et al. 2017).

Figure 5 shows the wavenumber–frequency spectrum of outgoing longwave radiation (OLR) in the boreal winter for the observations and simulations. The "MJO band" is displayed showing eastward propagation of the MJO with a period that ranges between 30 and 80 days. The observations indicate that the spectrum power of OLR is mainly concentrated in the MJO band. The dominant spatial scales of the zonal wave numbers of OLR are 1–3 waves (Fig. 5a). Compared to the observations, the OS experiment of BCC-CSM2-T159 simulates a weaker eastward power at wavenumbers 1–3. The spectral peak in the OS experiment of BCC-CSM2-T159 occurs at a lower frequency and over a larger range of wavenumbers compared to the observed peak (Fig. 5b). In comparison, the MS experiment of BCC-CSM2-T159 produces a stronger strength in the MJO band than the OS experiment, which is closer to the observations (Fig. 5c). The eastward propagation and spectral peak of the MJO are better reproduced

by the MS experiment than by the OS experiment of BCC-CSM2-T159.

To quantitatively evaluate the wavenumber–frequency spectrum of the MJO, the ratio of the eastward power to the westward power (E/W ratio), eastward power normalized by the observations (E/O ratio), and MJO periodicity (P_{WFPS}) within the MJO wavenumber–frequency ranges (period 30–80 days and wavenumbers 1–3) are calculated in the MS and OS experiments of BCC-CSM2-T159. The E/W ratio is determined by dividing the sum of the spectrum power in the MJO band by the sum of the corresponding westward power. It represents the robustness of the eastward propagation of the MJO (Zhang and Hendon 1997). The E/O ratio is obtained by normalizing the total of the simulated spectrum power in the MJO band by the counterpart of the observed power. The E/W ratio alone is not a sufficient assessment metric of the simulation capability for the eastward propagation of the MJO. The E/O ratio is complementary to the E/W ratio. P_{WFPS} is derived by dividing the total power-weighted period by the sum of the total power over 30–80 days, considering wavenumbers of 1–3.

As shown in Table 1, the E/W ratio of the OS experiment (3.79) is weaker than that of the observations (4.61), indicating that the eastward propagation is lower than the observations. The E/W ratio of the MS experiment (4.0) is improved and closer to the observations. The E/O ratio is 0.7 for the OS experiment and 1.07 for the MS experiment, indicating more reasonable eastward propagation in the

Fig. 5 November–April wave-number–frequency spectrum of OLR anomaly averaged over10° S–10° N. The vertical dashed lines indicate the MJO band (30–80 days). The eastward/westward power ratio (E/W ratio) and the eastward power normalized by the observations (E/O ratio) are shown in the top right of each panel. **a** NOAA/ERA5, **b** BCC-CSM2-T159 (OS), **c** BCC-CSM2-T159 (MS), **d** BCC-CSM2-T382 (OS), **e** BCC-CSM2-T382 (MS)
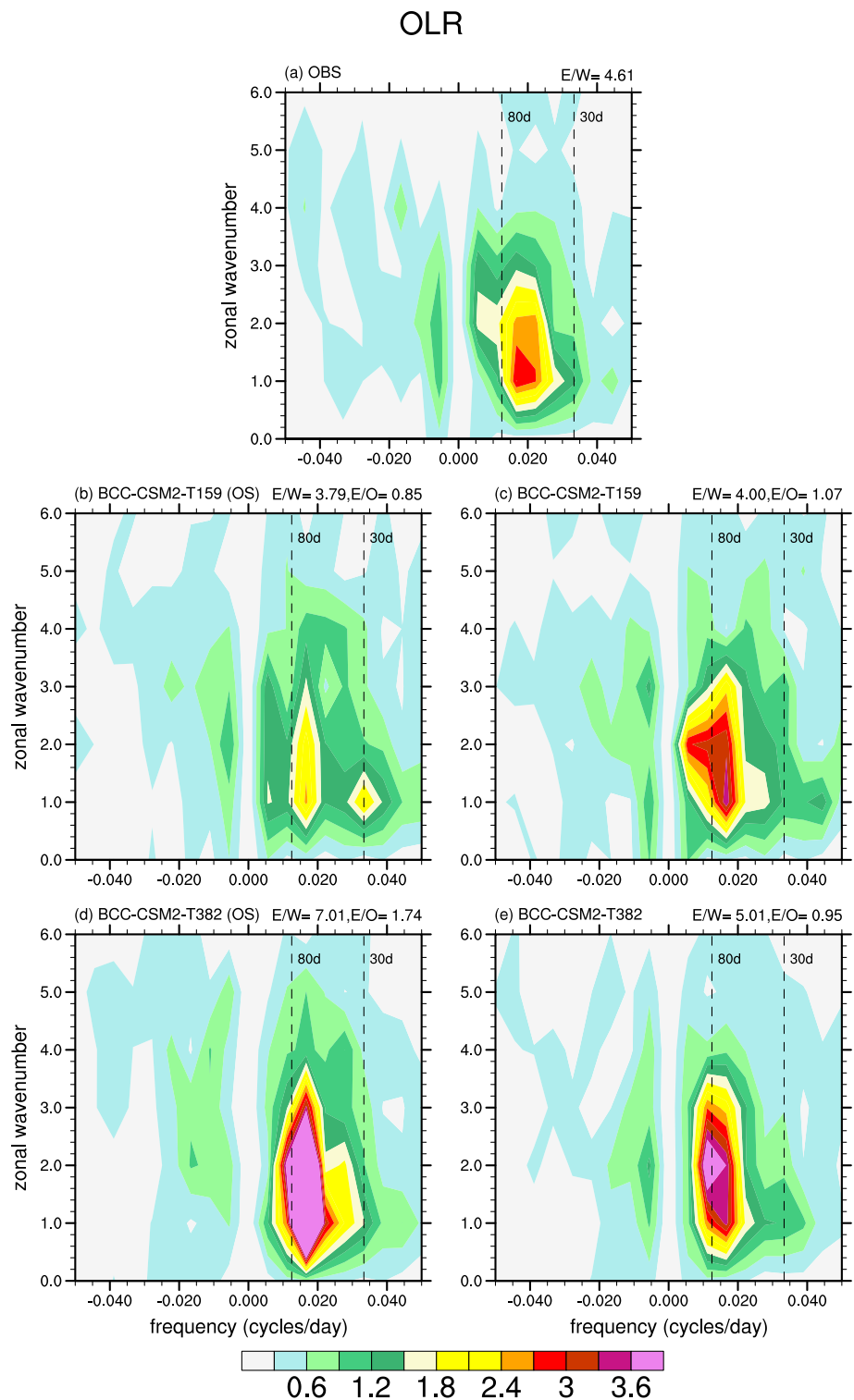
simulation with the modified deep convection scheme. The MS experiment increases the P_{WFPS} for the OLR (47.5), which is greater than that of the OS experiment (45.5) and closer to the observations (46.9).

The OS experiment of the high-resolution model BCC-CSM2-T382 overestimates the spectral intensity and eastward propagation of the OLR, which are much higher than those of the OS experiment of BCC-CSM2-T159 (Fig. 5d). The MS experiment of BCC-CSM2-T382 decreases the spectral intensity and eastward propagation relative to the OS experiment, and has closer E/W ratio and P_{WFPS} values to the observations (Table 1). The E/O

Table 1 Skill metrics representing MJO amplitude and MJO period

	E/W ratio			E/O ratio			P_{WFPS} (day)		
	OLR	U850	U200	OLR	U850	U200	OLR	U850	U200
Observation	4.61	4.29	3.65				46.9	48.2	46.0
BCC-CSM2-T159 (OS)	3.79	3.78	2.47	0.85	0.70	0.76	45.5	45.8	44.7
BCC-CSM2-T159 (MS)	4.00	3.34	2.76	1.07	0.80	0.77	47.5	46.3	46.0
BCC-CSM2-T382 (OS)	7.01	4.75	4.05	1.74	1.41	1.06	50.9	51.9	49.8
BCC-CSM2-T382 (MS)	5.01	4.78	2.44	0.95	0.82	0.66	49.2	50.7	49.0

E/W ratio, eastward/westward power ratio; E/O ratio, eastward power normalized by the observations; P_{WFPS}, dominant eastward period from the wavenumber–frequency power spectra within the MJO wavenumber–frequency ranges (period 30–80 days and wavenumbers 1–3)

OLR outgoing longwave radiation, *U850* 850-hPa zonal wind, *U200* 200-hPa zonal wind, *OS* the experiment with the original scheme, *MS* the experiment with the modified scheme

also exhibits an obvious improvement with values of 1.74 and 0.95 for the OS and MS experiments, respectively. These results demonstrate the benefits of the improved deep convection scheme for the simulation of the spectrum of the OLR in two models (BCC-CSM2-T159 and BCC-CSM2-T382).

Wavenumber–frequency spectra for 850-hPa zonal wind (U850) is shown in Fig. 6. The observations denote the eastward power in the period range of 30–80 days and at a zonal wavenumber of 1 (Fig. 6a). Similar to OLR, the OS experiment of BCC-CSM2-T159 underestimates the strength of the MJO band, while the OS experiment of BCC-CSM2-T382 overestimates the strength of the MJO band (Fig. 6b, d). With the improved deep convection scheme, the MS experiments of both BCC-CSM2-T159 and BCC-CSM2-T382 improve the simulations of the spectral strength and wavenumber (Fig. 6c, e). As shown in Table 1, the E/O ratio and P_{WFPS} in the MS experiment are improved compared to those in the OS experiment. However, in both BCC-CSM2-T159 and BCC-CSM2-T382, the MS experiment does not improve the E/W ratio compared to the OS experiment.

Figure 7 shows the wavenumber–frequency spectra for 200-hPa zonal wind (U200). The dominant zonal wave numbers are within 1 wave for U200 in the observations. The spectral peak of U200 occurs in the low frequency domain (50–80 days) (Fig. 7a). In the OS experiment of BCC-CSM2-T159, both the eastward power in the MJO band and the corresponding westward power are weaker than those in the observations (Fig. 7b). The MS experiment improves the simulation in both eastward power and the corresponding westward power (Fig. 7c), but not as much as those in OLR and U850. In the OS experiment of BCC-CSM2-T382, the spectral peak is stronger and is at a wider wavenumber range than the observations (Fig. 7d). With the improved deep convection scheme, the MS experiment of BCC-CSM2-T382 improves the simulations of the eastward power in the MJO band (Fig. 7e). The E/W ratio, E/O ratio, and P_{WFPS} of the eastward power can be better simulated in the MS experiment than in the OS experiment of BCC-CSM2-T159 (Table 1). However, the MS experiment of BCC-CSM2-T382 only shows a small improvement in P_{WFPS}. In addition, the E/O ratio and P_{WFPS} of U200 are less affected by the improved deep convection scheme than those of OLR and U850. This indicates that the modified deep convection scheme influences the upper troposphere less than the lower troposphere. One possible reason is that the improved deep convection scheme is achieved by altering the convective moisture, which is mainly concentrated in the lower troposphere.

Figures 5, 6, and 7 show the positive contribution of enhancing the resolution to the spectrum of the MJO simulations in the BCC-CSM2 model. However, the effects of the increased resolution on the simulation of the MJO spectrum differ among the climate models (Crueger et al. 2013; Malviya et al. 2018; Rajendran et al. 2008; Li et al. 2016). Several studies showed that increasing the resolution of the models enhances the spectrum of the MJO (Crueger et al. 2013; Malviya et al. 2018). Some other studies pointed out that the increase in the horizontal resolution does not help to increase the power in the MJO band (Rajendran et al. 2008; Li et al. 2016). Both stratiform and convection processes have impacts on the simulation of the MJO in the model. At present, we do not have an accurate understanding of the causes of MJO spectrum enhancement with increased horizontal resolution. In future work, we will conduct more experiments to investigate the underlying mechanism.

The CEOF analysis is performed using 20–100 days bandpass-filtered OLR, U850 and U200 data averaged between 15° S and 15° N. This analysis is based on the RMM method proposed by Wheeler and Hendon (2004). Figure 8 shows the two leading CEOFs from the observations and simulations. The order and sign of each mode of the simulations are adjusted to best match the observations. In the observations, the first (second) CEOF mode exhibits convective intensification (inhibition) over the tropical Indian Ocean and convective inhibition (intensification) over the eastern Pacific

Fig. 6 The same as Fig. 5 but for U850
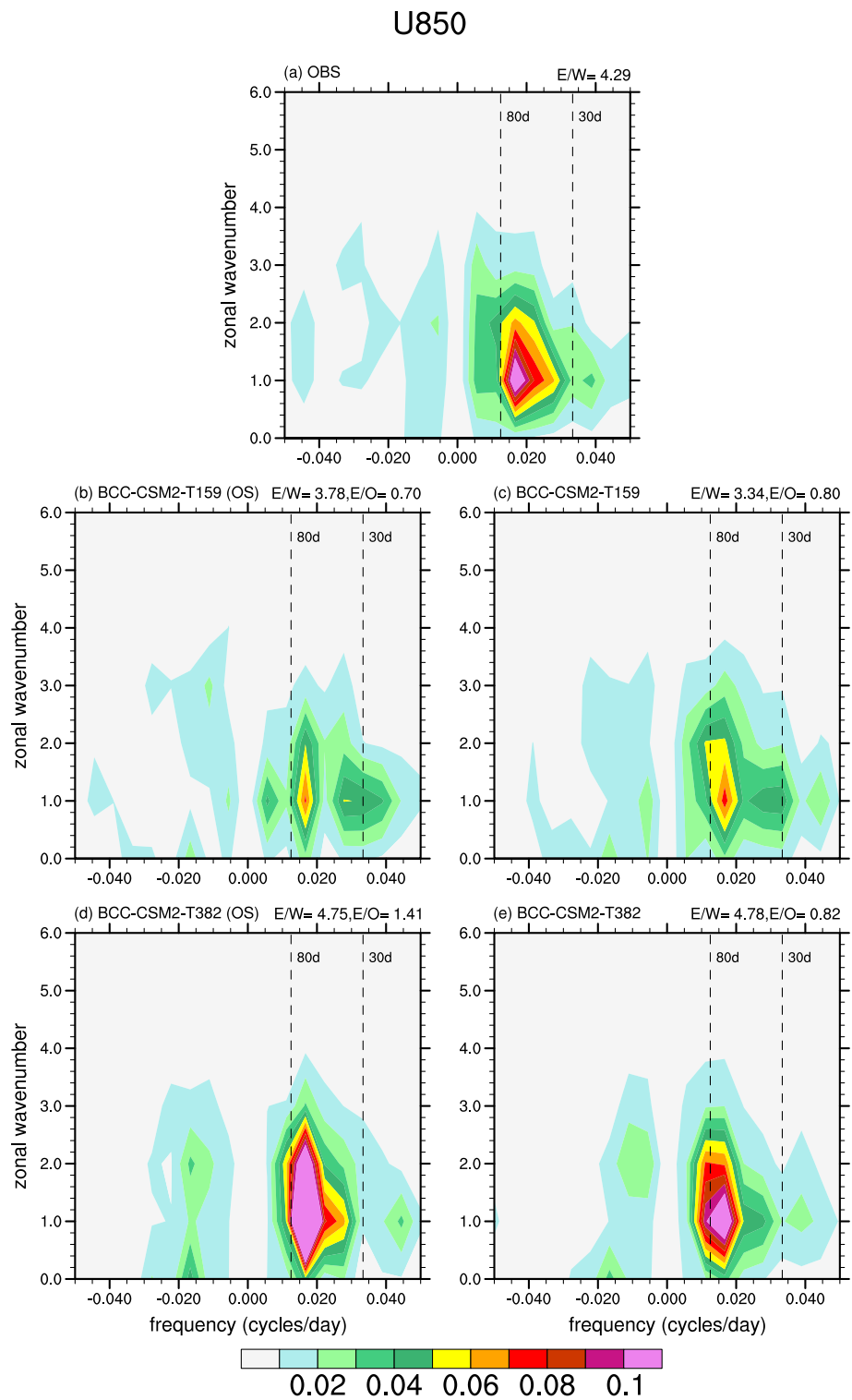
(Fig. 8a, b). The convection in both CEOF1 and CEOF2 is accompanied by low-level wind field convergence and high-level wind field divergence. In BCC-CSM2-T159, the first and second CEOF modes of the OS experiment show weaker convection and zonal wind strength compared to the observations (Fig. 8c, d). The peak convection of the

CEOF2 simulated by the OS experiment is located at 130° E, while it occurs at 150° E in the observations. Compared to the OS experiment, the MS experiment of BCC-CSM2-T159 improves simulations in the intensity and location of the peak convective signal, and the strength of the zonal wind. In the CEOF1 of BCC-CSM2-T382, the intensity and
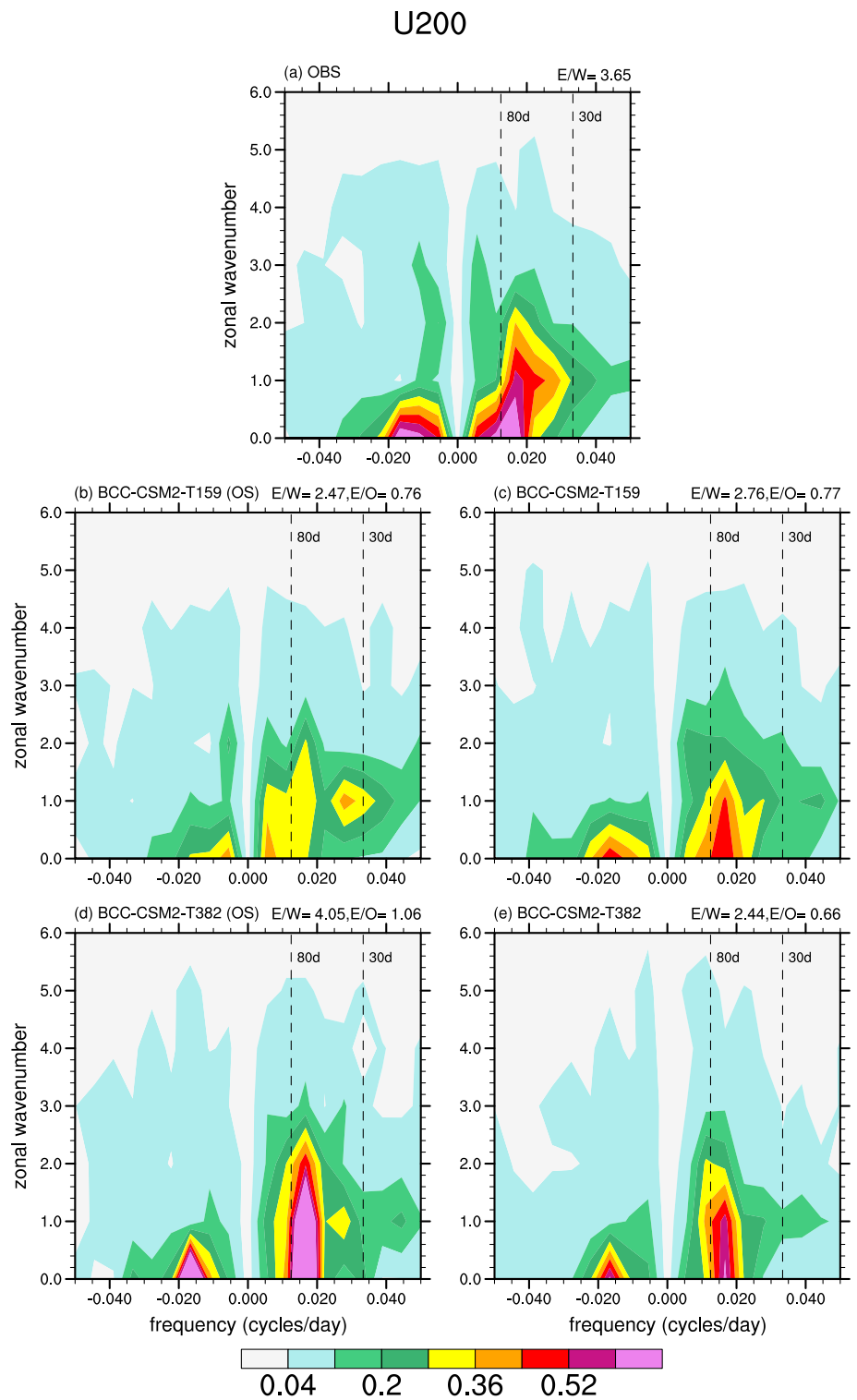
location of the convection in the Indian Ocean simulated by the MS experiment are closer to the observations than the OS experiment (Fig. 8e). However, the MS experiment of BCC-CSM2-T382 does not show improvement in simulating the spatial structure of CEOF2. The intensity of the CEOF2 peak convection is weaker over the western Pacific in the MS

experiment, and the peak location is westward relative to the observations and the OS experiment (Fig. 8f).

Table 2 presents the two MJO metrics from the CEOF analysis. The first metric is the percentage of the total variance (PCT) contributed by the first two CEOFs. In the observations, the two dominant CEOFs explain 42.87%
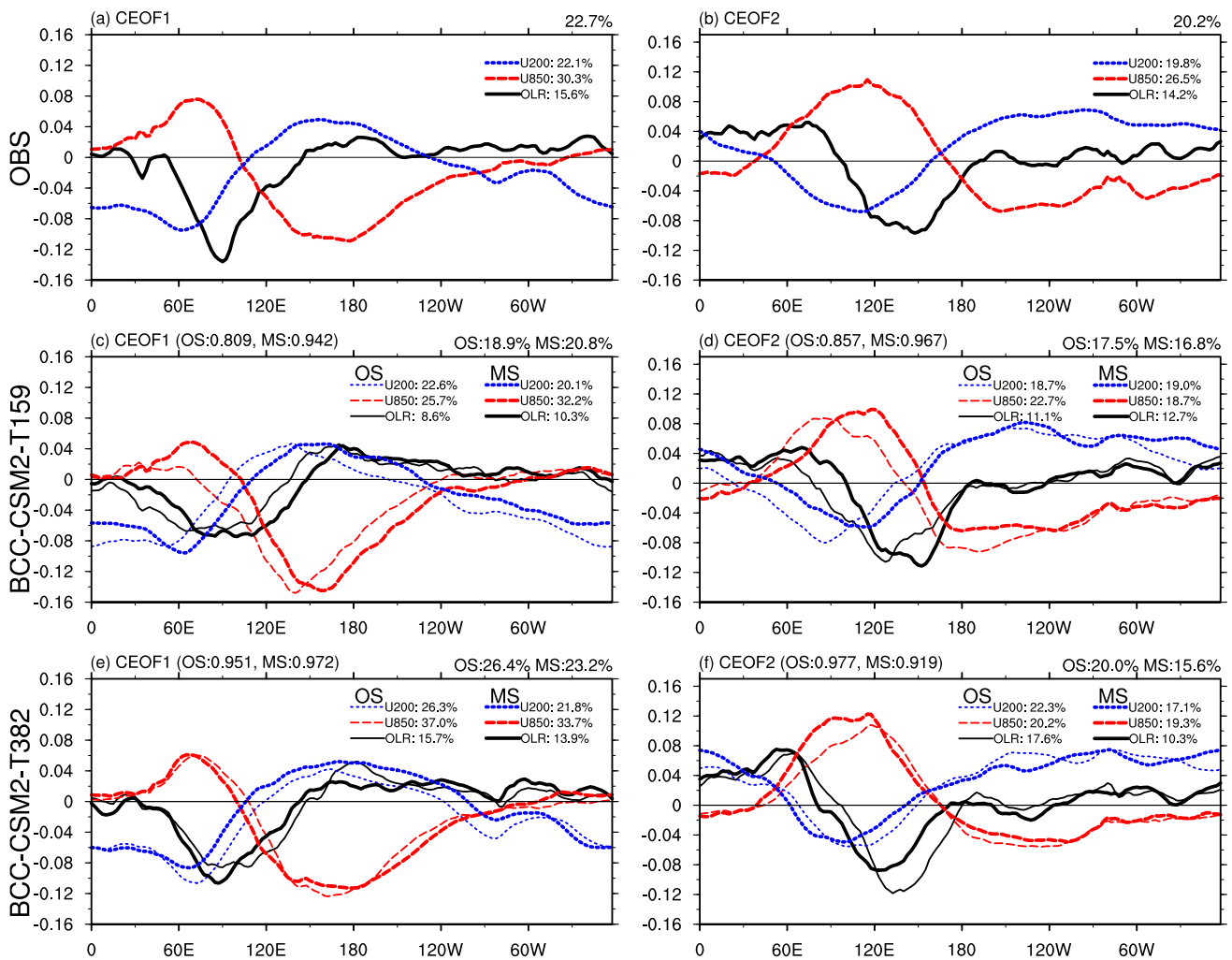
Fig. 8 Two leading CEOFs of 20–100-day filtered OLR, U850, and U200 averaged over 15° S-15° N in NOAA&ERA5 (**a, b**), BCC-CSM2-T159 (**c, d**), and BCC-CSM2-T382 (**e, f**). **a, c, e** are the first mode, and **b, d, f** are the second mode. The values in the upper left parentheses of each plot indicate the mean value of the correlation coefficients of the three variables (OLR, U850, and U200) between the observations and simulations. The explained variance of each mode is given in the top right of each plot. The legend of each panel shows the percentage variance explained by each mode of the three variables (OLR, U850, and U200). The thin curves and thick curves indicate the OS and MS experiments, respectively

of the total variance. The OS experiment of BCC-CSM2-T159 underestimates the mean PCT (36.43), and the PCTs of the three variables. There is some improvement in the mean PCT of the MS experiment (37.64), with increased explained variances in the variables of OLR and U850. The OS experiment of BCC-CSM2-T382 overestimates the mean

Table 2 Skill metrics representing MJO structure

	PCT (%)				C_SPATIAL			
	OLR	U850	U200	Mean	OLR	U850	U200	Mean
Observation	29.81	56.88	41.94	42.87				
BCC-CSM2-T159 (OS)	19.69	48.36	41.24	36.43	0.83	0.79	0.88	0.83
BCC-CSM2-T159 (MS)	22.97	50.89	39.05	37.64	0.93	0.95	0.98	0.96
BCC-CSM2-T382 (OS)	33.39	57.18	48.57	46.38	0.94	0.98	0.97	0.96
BCC-CSM2-T382 (MS)	24.26	53.07	38.94	38.76	0.90	0.98	0.96	0.95

PCT, the percentage variance explained by the two leading CEOFs (unit: %); C_SPATIAL, the spatial pattern correlation coefficient of the two leading CEOFs between the observations and simulations and their mean (Mean)

PCT (46.38) and the PCTs of the three variables, while the MS experiment underestimates the mean PCT (38.76) and the PCTs of the three variables. The mean PCT of the MS experiment in BCC-CSM2-T382 is closer to the observations than that of the MS experiment in BCC-CSM2-T159.

The second metric is the spatial correlation coefficient ($C_{SPATIAL}$) between the observations and simulations for the two dominant CEOFs. This metric is used to quantify the ability of the model to simulate the structure of CEOF modes. In the OS experiment of BCC-CSM2-T159, the mean values of $C_{SPATIAL}$ of OLR, U850, and U200 are 0.83, 0.79, and 0.88, respectively. With the modified scheme, the MS experiment increases the $C_{SPATIAL}$ of the three variables, with values of 0.93, 0.95, and 0.98 for OLR, U850, and U200 respectively. The greatest improvement is U850, indicating the prominent influence of the scheme in the lower troposphere. For the simulations of BCC-CSM2-T382, both the OS and MS experiments have high $C_{SPATIAL}$ above 0.9 for the three variables. The modified deep convection scheme has less influence on the structure of the MJO in BCC-CSM2-T382 than that in BCC-CSM2-T159.

The lead-lag correlations of the two leading principal component time series (PCs) are shown in Fig. 9, which are created by applying filtered anomalous fields to the corresponding CEOF modes. In the observations, the first CEOF mode (convection center over the east Indian Ocean) is 10 days ahead of the second CEOF mode (convection center over the west Pacific). The OS and MS experiments of both BCC-CSM2-T159 and BCC-CSM2-T382 can reproduce the lead-lag relationship between the two dominant CEOF modes. The correlations between the simulations and the observed lead-lag correlation are all above 0.96.

To estimate the coherency of the propagation and periodicity of the MJO from the lead-lag correlations shown in Fig. 9, we calculate the mean of the absolute values of the maximum and minimum lead-lag correlation coefficients (C_{MAX}) and the dominant eastward period (P_{CEOF}). P_{CEOF} is obtained by multiplying the period between the maximum positive correlation and the maximum negative correlation by 2. The C_{MAX} of the observation is 0.77, while the value is 0.77 and 0.78 in the OS experiments of BCC-CSM2-T159 and BCC-CSM2-T382, respectively. The MS experiments of both BCC-CSM2-T159 and BCC-CSM2-T382 have slightly lower C_{MAX}. The P_{CEOF} in the OS experiment of BCC-CSM2-T159 (BCC-CSM2-T382) is 34 days (42 days), which is smaller (larger) than the observations (40 days). The MJO periods simulated by the MS experiments of both BCC-CSM2-T159 and BCC-CSM2-T382 are closer to the observations (see Table 3).
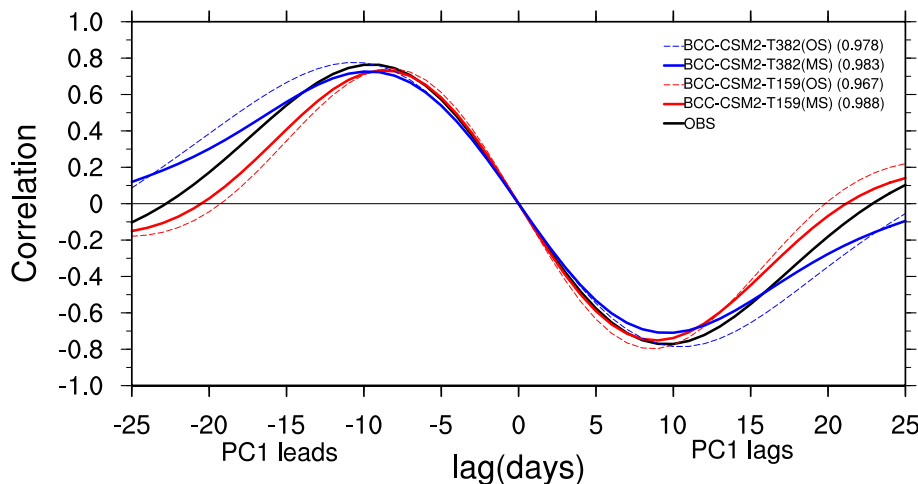
3.3 Propagation of the MJO

We further evaluate the model's ability to simulate the propagation of the MJO. The eastward propagation diagram of the MJO is shown by the lead-lag correlations of the intraseasonal anomalies (20–100 days) of OLR and U850 averaged over 10° S–10° N, with respect to the MJO convection center in the Indian Ocean region (5° S–5° N, 75°–85° E) (Fig. 10). In the observations, the MJO shows clear eastward

Table 3 Skill metrics representing the coherency of MJO propagation and MJO periodicity from the lead-lag correlations between the PCs of the two leading modes

	C_{MAX}	P_{CEOF} (day)
Observation	0.77	40
BCC-CSM2-T159 (OS)	0.77	34
BCC-CSM2-T159 (MS)	0.74	36
BCC-CSM2-T382 (OS)	0.78	42
BCC-CSM2-T382 (MS)	0.72	40

C_{MAX} the average of the absolute values of the maximum and minimum lead-lag correlation coefficients, P_{CEOF} the dominant eastward period from the first two CEOF modes (unit: day)

Fig. 9 Lead-lag correlation coefficients between the first and second principal component time series corresponding to the first two CEOF modes in the observations, and simulations of BCC-CSM2-T159 (OS), BCC-CSM2-T159 (MS), BCC-CSM2-T382 (OS) and BCC-CSM2-T382 (MS). The values in the upper right parentheses show the spatial correlation between the observations and simulations

propagation from the Indian Ocean to the Pacific Ocean, with a speed of approximately 5 m/s (Fig. 10a). The OS and MS experiments of both BCC-CSM2-T159 and BCC-CSM2-T382 capture the eastward propagation feature of the MJO, but with differences in the strength of the MJO. Compared to the observations, the MJO in the OS experiment of BCC-CSM2-T159 is obviously weaker than the observed over the equatorial Indo-Pacific regions, and becomes discontinuous after propagating to the western Pacific (Fig. 10b). In contrast, both the strength and propagation continuity of the MJO are improved in the MS experiment (Fig. 10c). The

MS experiment of BCC-CSM2-T159 produces higher PCC and lower RMSE values than the OS experiment (Table 4). In the OS experiment of BCC-CSM2-T382, the intensity of the MJO is overestimated and stronger than the observations (Fig. 10d). The MS experiment of BCC-CSM2-T382 decreases the intensity of the MJO, and has a higher PCC skill and lower root mean square error (RMSE) (Table 4). This indicates that the modified deep convection scheme in both BCC-CSM2-T159 and BCC-CSM2-T382 can improve the simulations in the intensity and eastward propagation feature of the MJO over the equatorial Indo-Pacific regions.
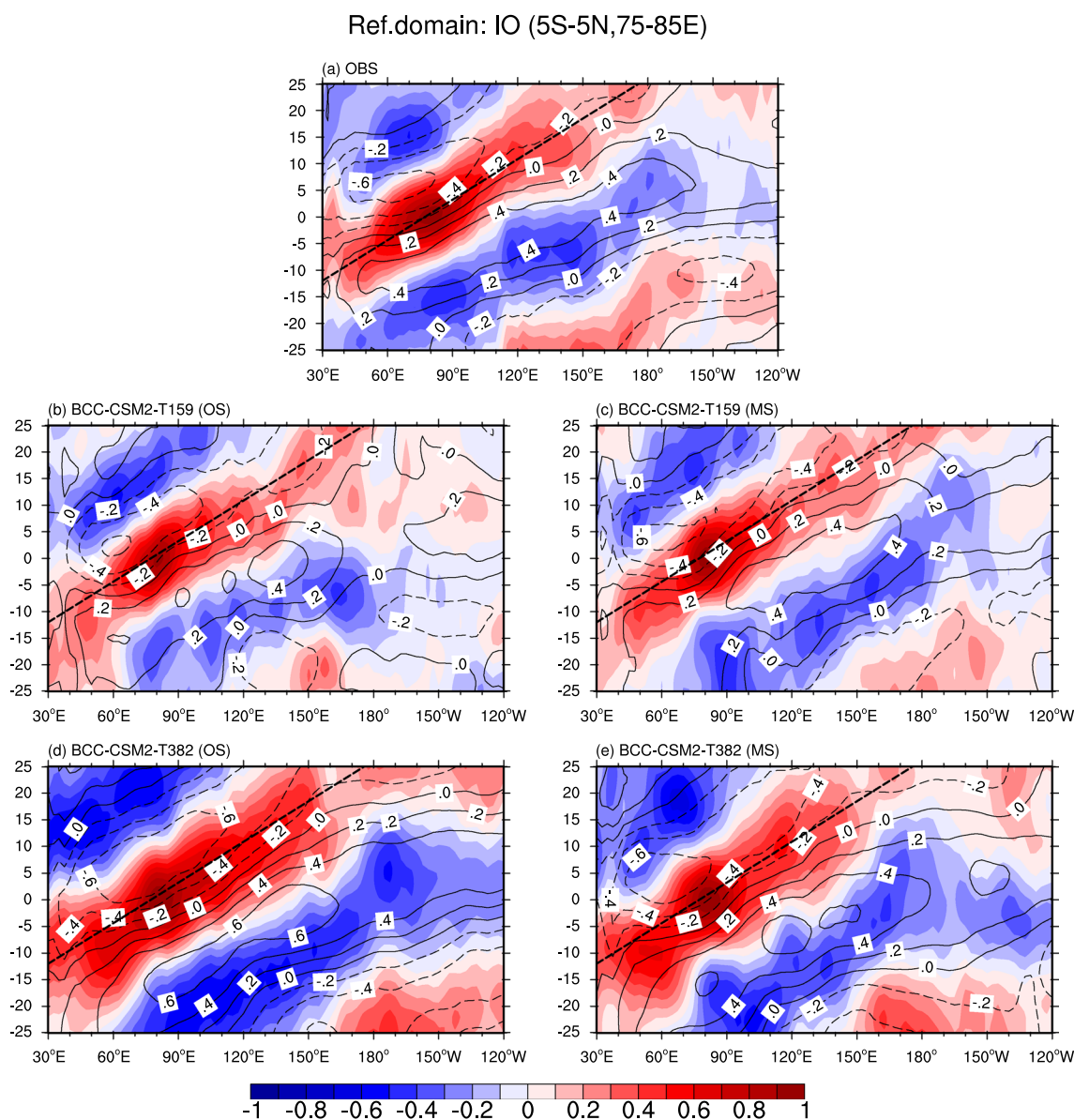

Fig. 10 Eastward propagation of the MJO shown as the lead-lag correlation of 20–100 days filtered OLR (shading) and U850 (contour) averaged over 10° S–10° N with reference to itself over the equatorial eastern Indian Ocean (IO, 5° S–5° N, 75°–85° E) in **a** NOAA&ERA5, **b** BCC-CSM2-T159 (OS), **c** BCC-CSM2-T159 (MS), **d** BCC-CSM2-T382 (OS), and **e** BCC-CSM2-T382 (MS) from November–April. The dashed straight line denotes the eastward propagation speed of 5 m s.$^{-1}$

Table 4 Skill metrics representing eastward propagation of MJO

	IO		WP		MJO eastward propagation skill
	PCC	RMSE	PCC	RMSE	
BCC-CSM2-T159 (OS)	0.869	0.164	0.940	0.127	0.905
BCC-CSM2-T159 (MS)	0.908	0.139	0.962	0.101	0.935
BCC-CSM2-T382 (OS)	0.830	0.235	0.933	0.163	0.882
BCC-CSM2-T382 (MS)	0.866	0.178	0.915	0.147	0.891

PCC and RMSE denote the spatial correlation coefficient, and the root mean square error between the observations and simulations of the lead-lag correlations of the intraseasonal anomalies (20–100 days) of the outgoing longwave radiation in the lag-longitude domain (60° E–180°, day – 20 to day 20), respectively. MJO eastward propagation skill is measured by averaging the PCC skills in two regions (IO and WP)

Figure 11 shows the eastward propagation diagrams of the MJO with reference to the MJO convection center in the Western Pacific region (5° S–5° N, 130°–150° E). The observed MJO convective signal propagates eastward from the East Indian Ocean and decays near the dateline in the observations (Fig. 11a). The OS experiment of BCC-CSM-MR simulates a weaker MJO signal and smaller propagation ranges than the observations (Fig. 11b). In contrast, the MS experiment of BCC-CSM2-T159 can reproduce more reasonable propagation of the MJO (Fig. 11c). In particular, the MS experiment can reproduce the feature of the MJO convection decaying near the dateline. The MS experiment of BCC-CSM2-T159 has a higher PCC skill and lower RMSE value than the OS experiment (Table 4). In BCC-CSM2-T382, the OS experiment produces an excessively strong MJO signal and low speeds (Fig. 11d). Although the MS experiment decreases the RMSE, it does not increase the PCC skill.

Table 4 also presents the MJO eastward propagation skill of the simulation, which is determined by the mean PCC skill for eastward MJO propagation in the two key reference regions. It is more reflective of the overall propagation skill than measurements of a single reference region (Wang and Lee 2017). The eastward propagation skill of BCC-CSM2-T159 (BCC-CSM2-T382) is improved from 0.905 (0.882) to 0.935 (0.891) by modifying the deep convection scheme. This suggests that both BCC-CSM2-T159 and BCC-CSM2-T382 models with the improved deep convection scheme generate more systematic eastward propagations and are closer to the observations.

The composite MJO life cycle of U850 and OLR anomalies in the boreal winter in the tropics is shown in Fig. 12, presenting the temporal and spatial evolution features of MJO convection. In the observations, MJO convection

(negative OLR anomaly) originates in the western Indian Ocean in the second phase and gradually enhances as it propagates eastward, reaching a maximum on the maritime continent. Then, the convection gradually weakens in the second half stage and ends in the western Pacific in the eighth phase (Fig. 12a). Similar features are found in the wind field. In contrast, the intensity of MJO convection over the maritime continent is underestimated by the OS experiment of BCC-CSM2-T159 in the active MJO phase, especially in phases 4–6. In addition, the OS experiment does not capture the weakening feature in the latter half of the MJO life cycle (Fig. 12b). Compared to the OS experiment, the convective transition from wet-to-dry phases can be reasonably simulated by the MS experiment, in agreement with the observations (Fig. 12c). For BCC-CSM2-T382, the convective intensity and spatial extent of the MJO simulated by the OS experiment are overestimated throughout the MJO life cycle. The same problem also appears in the positive OLR anomaly (Fig. 12d). Comparatively, the MS experiment in BCC-CSM2-T382 shows better simulations in both the wet phases and dry phases of the MJO (Fig. 12e). In addition, with the improved deep convection scheme, the temporal and spatial evolution features of the MJO reproduced by BCC-CSM2-T382 are closer to the observations than BCC-CSM2-T159.

3.4 MJO simulations without air–sea interaction

To better understand the impacts of the improved deep convection scheme and air–sea interactions on MJO simulations in the BCC-CSM2-T159 and BCC-CSM2-T382 models, the corresponding AMIP experiments are conducted using BCC-AGCM3-T159 and BCC-AGCM3-T382.

Figure 13 shows the wavenumber–frequency spectra of U850 for BCC-AGCM3 models. The spectral peak in the OS experiment of BCC-AGCM3-T159 does not occur in the MJO band but at a lower frequency. The OS experiments of both BCC-AGCM3-T159 and BCC-AGCM3-T382 underestimate the spectral strength of the MJO band. In contrast, the MS experiments for both BCC-AGCM3-T159 and BCC-AGCM3-T382 improve spectral strength in the MJO band. The E/W ratios, the E/O ratios, and P_{WFPS} of the MS experiments are improved compared to the OS experiments in BCC-AGCM3 models.

The eastward propagation of the MJO in BCC-AGCM3 models with reference to the MJO convective center in the Indian Ocean region is given in Fig. 14. The MJO in the OS experiment of BCC-AGCM3-T159 cannot propagate eastward across the oceanic continent and does not show a continuous eastward propagation feature. The OS experiment of BCC-AGCM3-T382 also shows weak propagation strength and a small propagation range. Consistent with the results of the coupled models, there is a significant
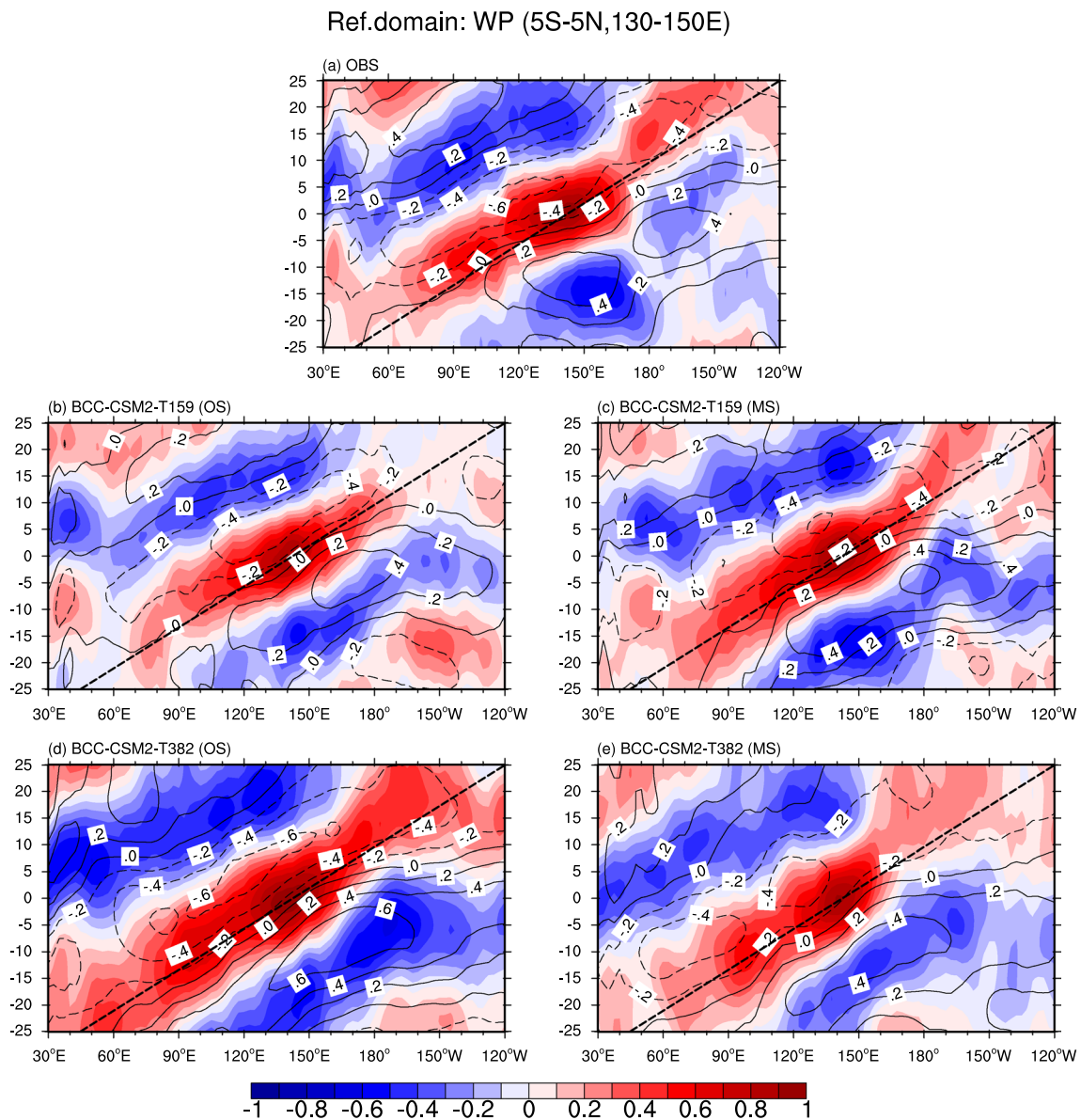
Ref.domain: WP (5S-5N,130-150E)

Fig. 11 The same as Fig. 10 but over the equatorial western Pacific (WP, 5° S–5° N, 130°–150° E)

improvement in the strength, propagation range and propagation continuity of the MJO of the MS experiments compared to the OS experiments in both BCC-AGCM3-T159 and BCC-AGCM3-T382.

Figures 13 and 14 demonstrate that the improved deep convection scheme also contributes to better MJO simulations in BCC-AGCM3 models. The performances on MJO simulations of both BCC-AGCM3-T159 and BCC-AGCM3-T382 are worse than those of the corresponding coupled models. This suggests that atmosphere–ocean interactions are important for MJO simulations in BCC models.

3.5 Physical mechanisms related to the improved MJO skill

The above analysis shows that both BCC-CSM2-T159 and BCC-CSM2-T382 with the modified deep convection scheme perform better in reproducing the major features of the MJO, including spectrum, period, intensity, eastward propagation and life cycle. To better understand the physical mechanism of these improvements, we analyze the moisture and atmospheric circulation related to the MJO in the MS experiments of BCC-CSM2-T159 and BCC-CSM2-T382. We select a typical strong MJO event (RMM > 1.0) propagating from the Indian Ocean to the western Pacific Ocean during the boreal winter in the observations (Fig. 15a), and

Fig. 12 November–April composite intraseasonal anomalies (20–100 days) of OLR (shading, unit: W m^{-2}) and 850-hPa wind (vector, unit: m s^{-1}) as a function of the MJO phase in **a** NOAA&ERA5, **b** BCC-CSM2-T159 (OS), **c** BCC-CSM2-T159 (MS), **d** BCC-CSM2-T382 (OS), and **e** BCC-CSM2-T382 (MS). The reference vector unit is meters per second (m s^{-1}) in the top right corner of each panel. The bottom right of each plot shows the phase and the number of days used to generate the phase
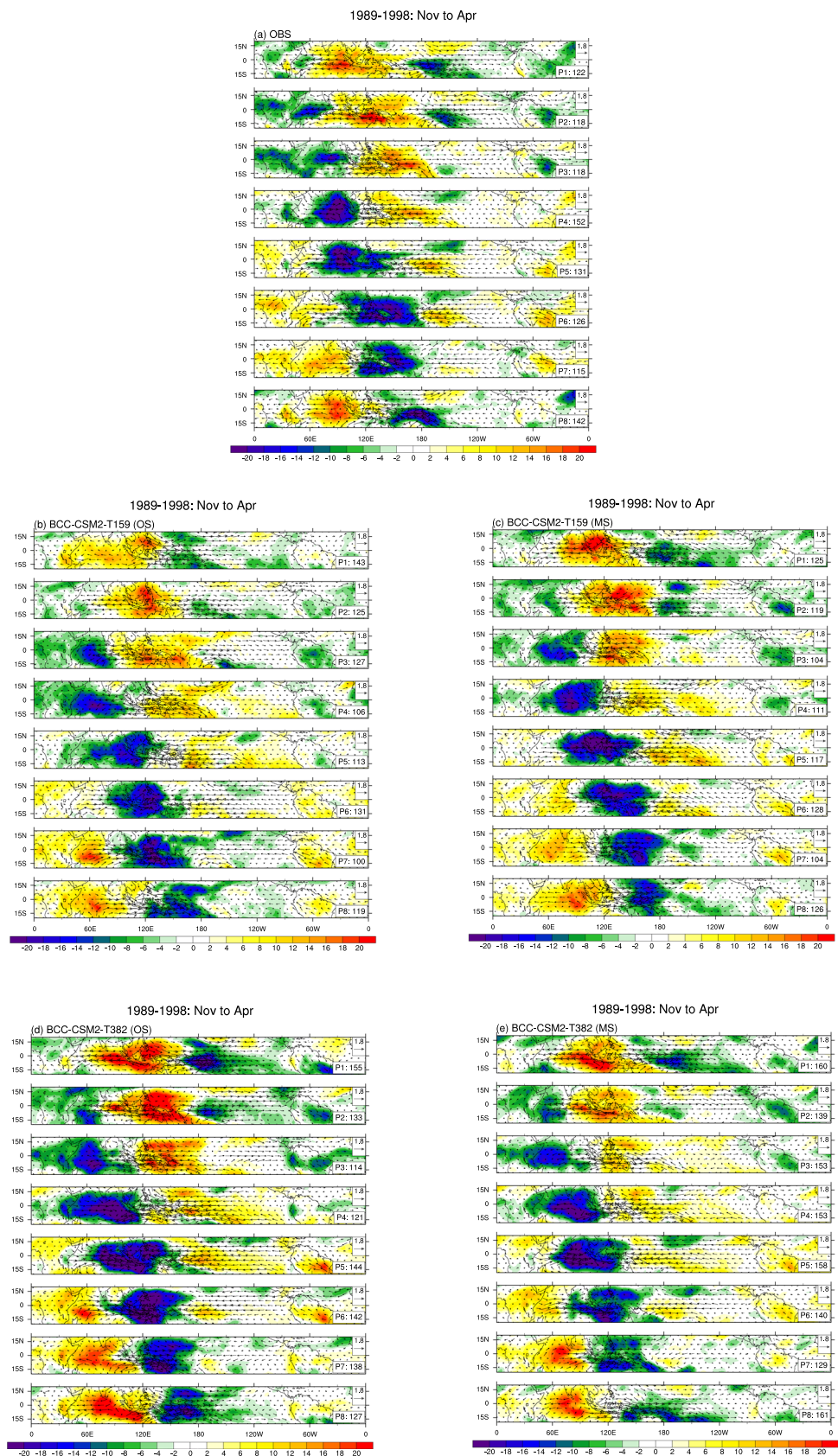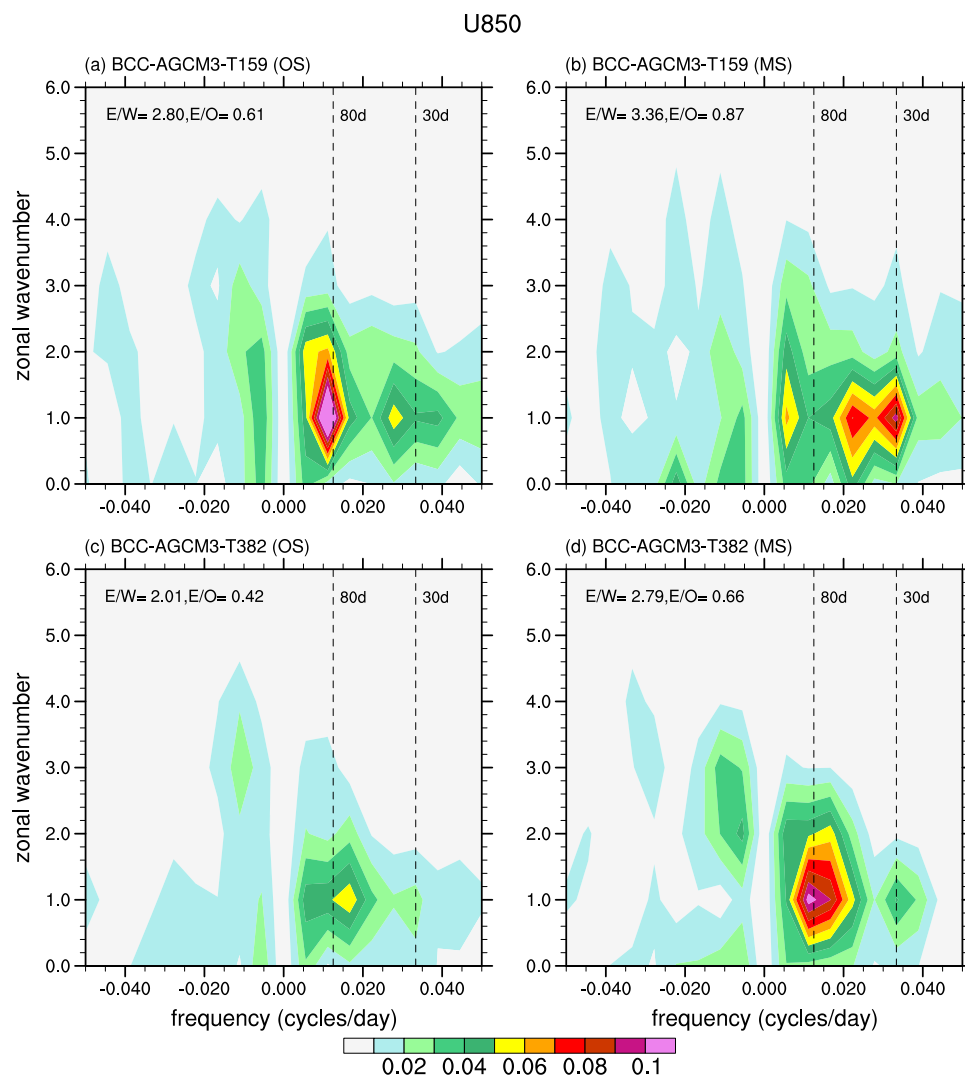
Fig. 13 The same as Fig. 6 but for BCC-AGCM3 models

U850

(a) BCC-AGCM3-T159 (OS) E/W= 2.80,E/O= 0.61

(b) BCC-AGCM3-T159 (MS) E/W= 3.36,E/O= 0.87

(c) BCC-AGCM3-T382 (OS) E/W= 2.01,E/O= 0.42

(d) BCC-AGCM3-T382 (MS) E/W= 2.79,E/O= 0.66

the MS experiments of BCC-CSM2-T159 (Fig. 16a) and BCC-CSM2-T382 (Fig. 17a), respectively. The selected MJO events all occur in the Indian Ocean, considering that the Indian Ocean is the initiation and enhancement zone of MJO events.

The vertical structures of the moisture tendency and circulation field averaged over 10° S-10° N corresponding to the three reference dates of P1, P2 and P3 in the observations are shown in Fig. 15. The moisture tendency includes the variations of water vapor in the atmosphere caused by all physical and dynamical processes. The lower part of each subplot shows the latitudinal distribution of the precipitation averaged over 10° S-10° N on the corresponding date. To realistically reflect the convection structure, these data are not filtered. The vertical dashed line represents the longitude position of the MJO convection center, which is jointly determined by the location of the maximum precipitation in the Indian Ocean region and the MJO phase. In the observations, the MJO convection center has obvious

eastward propagation over time (Fig. 15b–d). On date P1, there is an apparent positive water vapor transport in the lower troposphere (1000–700 hPa) to the east of the MJO convective center and strong upward motions in the middle troposphere (700–500 hPa) near the convective center (Fig. 15b). Meanwhile, there are strong westerly winds in the upper troposphere (500–300 hPa) and downdrafts to the east of the convective center, forming a vertical circulation circle. Such the vertical circulation circle also appears associated with the MJO convection center on dates P2 and P3 (Fig. 15c, d). For the selected MJO event simulated by the MS experiments of BCC-CSM2-T159 (Fig. 16b–d) and BCC-CSM2-T382 (Fig. 17b–d), the MJO convection center also moves eastward from dates P1 to P3, with similar structures of water vapor and vertical circulation circle near the MJO convention center. This indicates that the moisture transport processes can be realistically reproduced by the two models with the modified deep convection scheme.
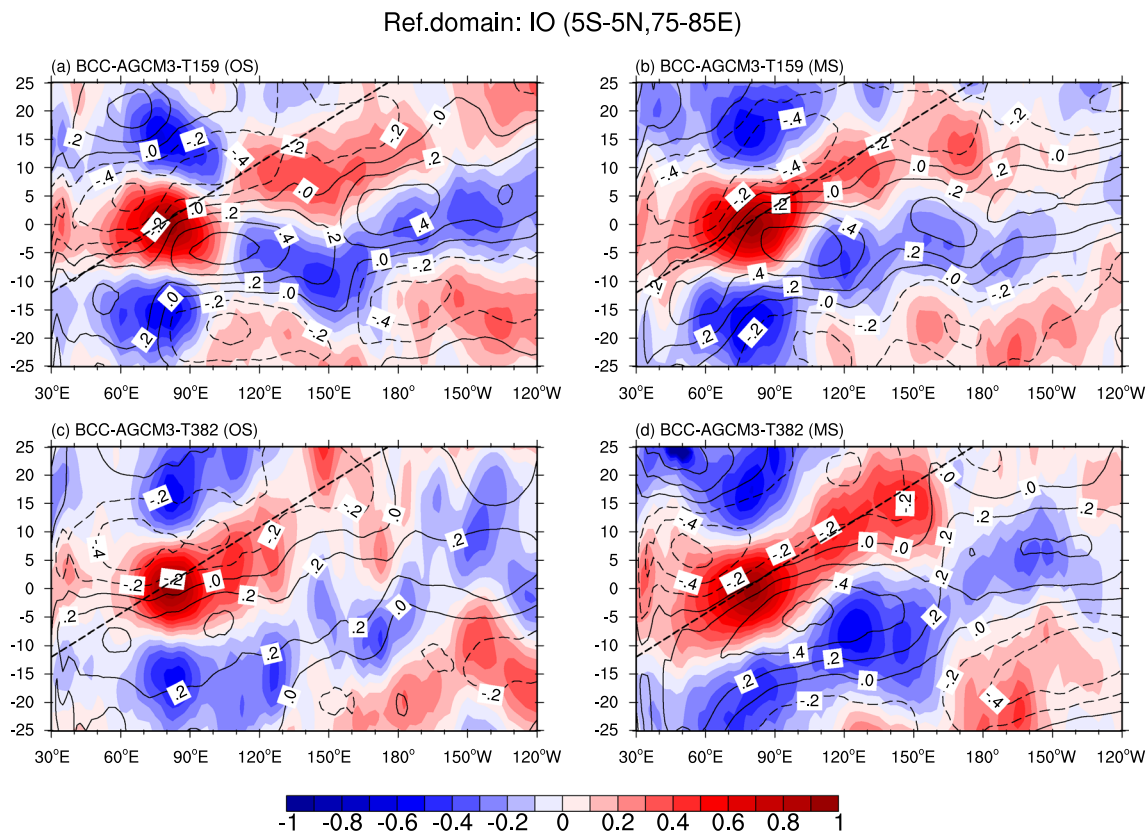
Fig. 14 The same as Fig. 10 but for BCC-AGCM3 models

To more clearly show the water vapor and vertical circulation circle structures near the center of the MJO, we select 7, 7 and 6 strong MJO events from the observations, the MS experiments of BCC-CSM2-T159 and BCC-CSM2-T382, respectively. These MJO convections are composited as day 0 when they reach 85° E. The composite vertical structure of the moisture tendency and the circulation field for multiple strong MJO events propagating eastward to 85° E are shown in Fig. 18. When the maximum composite MJO convection arrives at 85° E, the composite vertical structure to the east of the convective center in the MS experiments of both BCC-CSM2-T159 and BCC-CSM2-T382 exhibits the above vertical circulation circle (Fig. 18b, c), similar to the observations (Fig. 18a).

Based on the modified deep convection scheme and the diagnostics for moisture and atmospheric circulation, the physical mechanism can be summarized as follows. The original deep convection scheme, where convection mainly occurs in the same location grid air column, lacks the interaction between adjacent grid boxes. With increased horizontal resolution, such interaction cannot be ignored. Based on the structure

of MJO convection, the effects between adjacent grid boxes are parameterized as two key processes, including advection and downward transport processes. The newly developed deep convection scheme adds these two processes to the original scheme. After the initiation of MJO convection, the easterly winds in the lower troposphere and updrafts in the middle troposphere transport moisture from the lower troposphere to the upper troposphere. The water vapor in the upper troposphere is then transported to the lower troposphere to the east of the MJO convection center by advection and downward transport processes. This strengthens the moisture exchange from the lower troposphere to the upper troposphere around the convective cloud. The combined effects of the two processes promote moisture convergence to the east of the convention center in the lower troposphere, inducing eastward propagation of the MJO. Therefore, we can infer that the advection and downward transport processes in the modified scheme are the main reasons for the realistic simulations of the propagation and life cycle of the MJO.

Fig. 15 RMM phase diagram corresponding to a typical MJO east- ▶ ward propagation case in the observations (**a**). The RMM index of the panel (**a**) is calculated from NOAA & ERA5. The MJO event corresponding to panel (**a**) begins on 30 January 1990 and ends on 10 March 1990. The three black dots represent the three selected reference dates corresponding to MJO convection occurring in the Indian Ocean. P1 in panel (a) corresponds to 5 February 1990, P2 is 11 February 1990, and P3 is 16 February 1990. **b–d** Longitude–height cross–sections of specific humidity tendency (shading, unit: g kg^{-1} day^{-1}) overlaid with wind vectors (u, w) and longitudinal distribution of precipitation (unit: mm day^{-1}) on P1, P2, and P3, all averaged over 10° S–10° N. The number in the upper left parentheses of each panel represents the longitude position of the maximum precipitation center and is marked with a dashed vertical line in each panel. The dates corresponding to P1, P2, and P3 are marked in the upper middle of each panel

4 Summary and discussion

In this study, we investigate the effects of a modified deep convection scheme on the ability to simulate the MJO using the medium-resolution model BCC-CSM2-T159 and the high-resolution model BCC-CSM2-T382. Based on the original deep convection scheme, the modified scheme involves the transport processes of deep convective cloud water. The detrainment for liquid cloud water is horizontally transferred to neighboring grids, and a portion of the cloud water that is horizontally transported is allowed to be transported downward into the lower troposphere. Ten years simulations are conducted by BCC-CSM2-T159 and BCC-CSM2-T382 using the original deep convection scheme (OS) and the modified deep convection scheme (MS), respectively. The corresponding AMIP experiments are also conducted for the same decade using BCC-AGCM3-T159 and BCC-AGCM3-T152. The impacts of sea–air interactions on the MJO simulations in BCC-AGCM3 models are also investigated in this study. Performances of the OS and MS experiments are compared in simulating the basic features of the MJO.

The spectral analysis shows that BCC-CSM2-T159 and BCC-CSM2-T382 using the original deep convection scheme underestimate and overestimate the spectrum of the MJO, respectively. Both BCC-CSM2-T159 and BCC-CSM2-T382 using the modified deep convection scheme can more realistically simulate the spectrums of the MJO, especially in OLR and U850. Both BCC-CSM2-T159 and BCC-CSM2-T382 models with the improved deep convection scheme have more systematic eastward propagations that are closer to the observations. The spatial and temporal evolutionary features of MJO convection throughout the MJO life cycle are also improved in BCC-CSM2-T159 and BCC-CSM2-T382 with the improved deep convection scheme. The corresponding AMIP experiments indicate that both BCC-AGCM3-T159 and BCC-AGCM3-T382 using the improved deep convection scheme can improve simulation of the propagation, spectrum, and period of the MJO. The
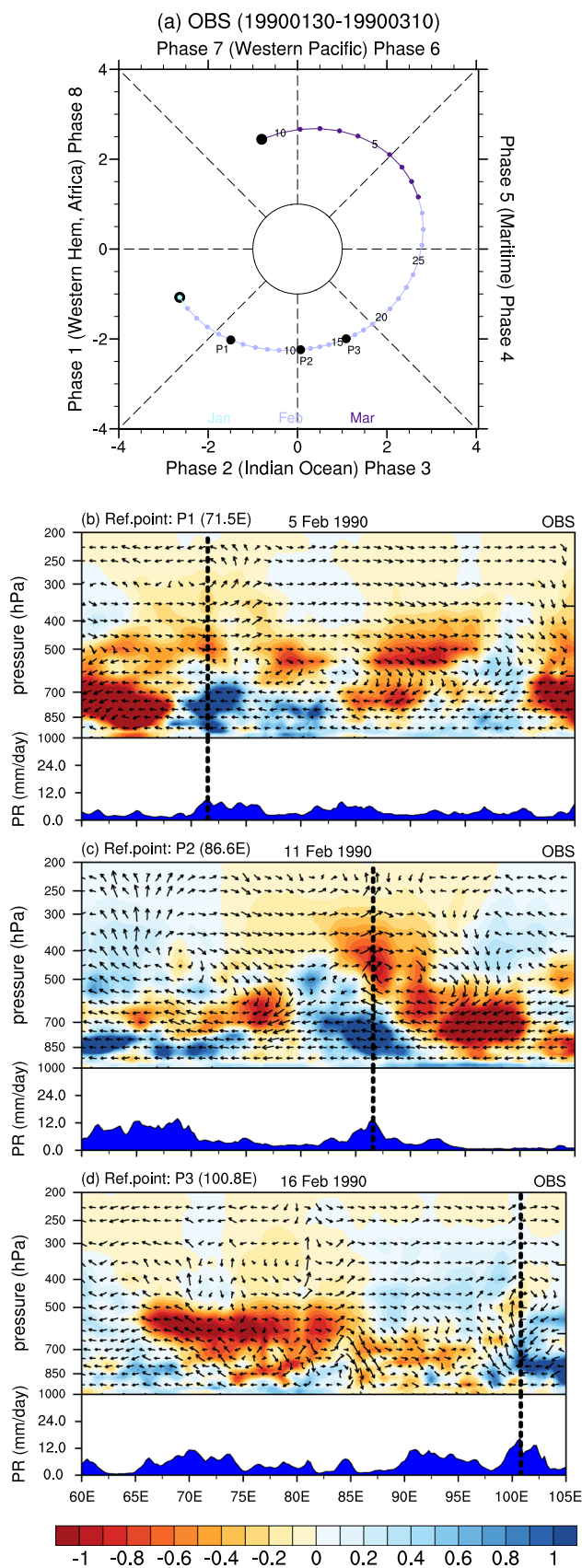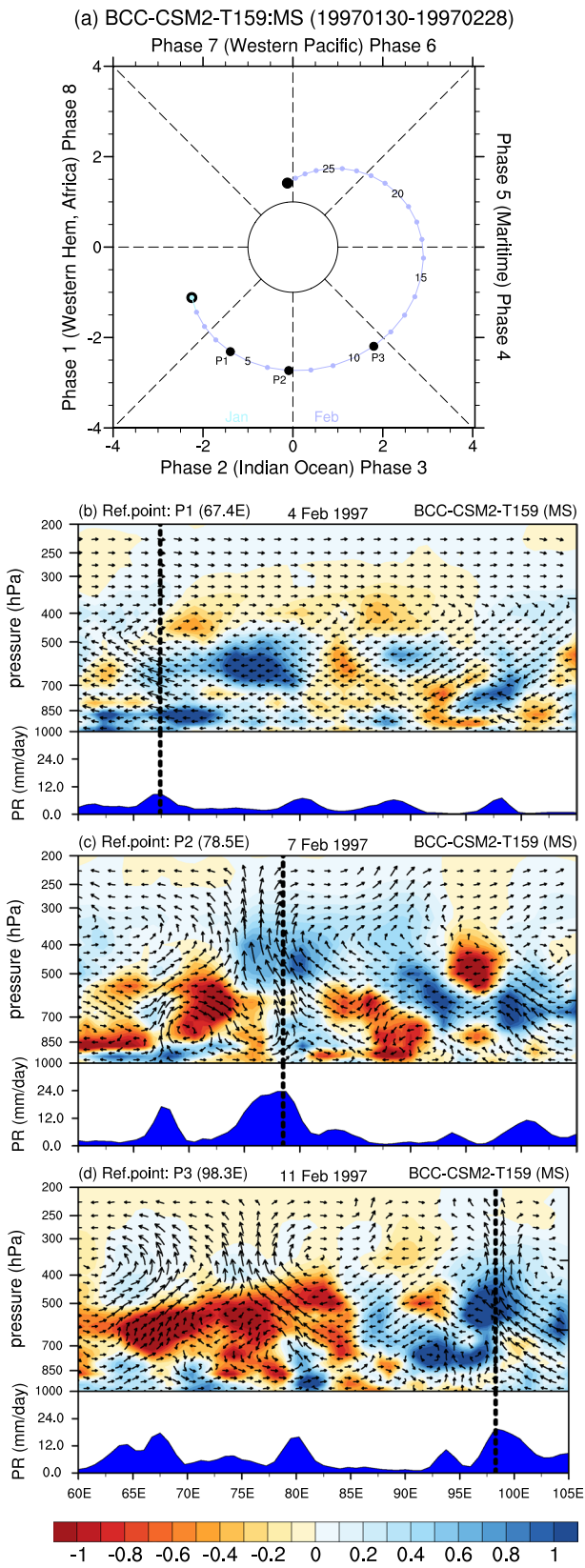
Fig. 16 The same as Fig. 15 but from the simulations of BCC-CSM2-T159 (MS). P1 in the panel corresponds to 4 February 1997, P2 is 7 February 1997 and P3 is 11 February 1997
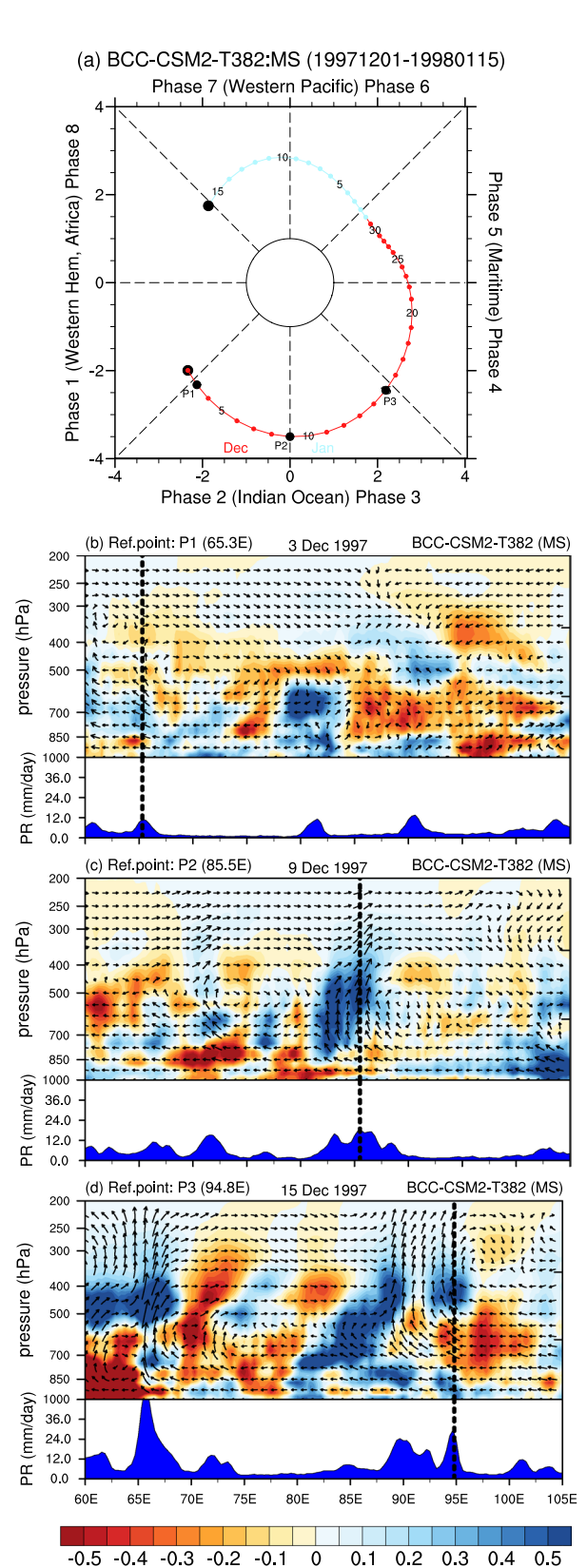
Fig. 17 The same as Fig. 15 but from the simulations of BCC-CSM2-T382 (MS). P1 in the panel corresponds to 3 December 1997, P2 is 9 December 1997, and P3 is 15 December 1997
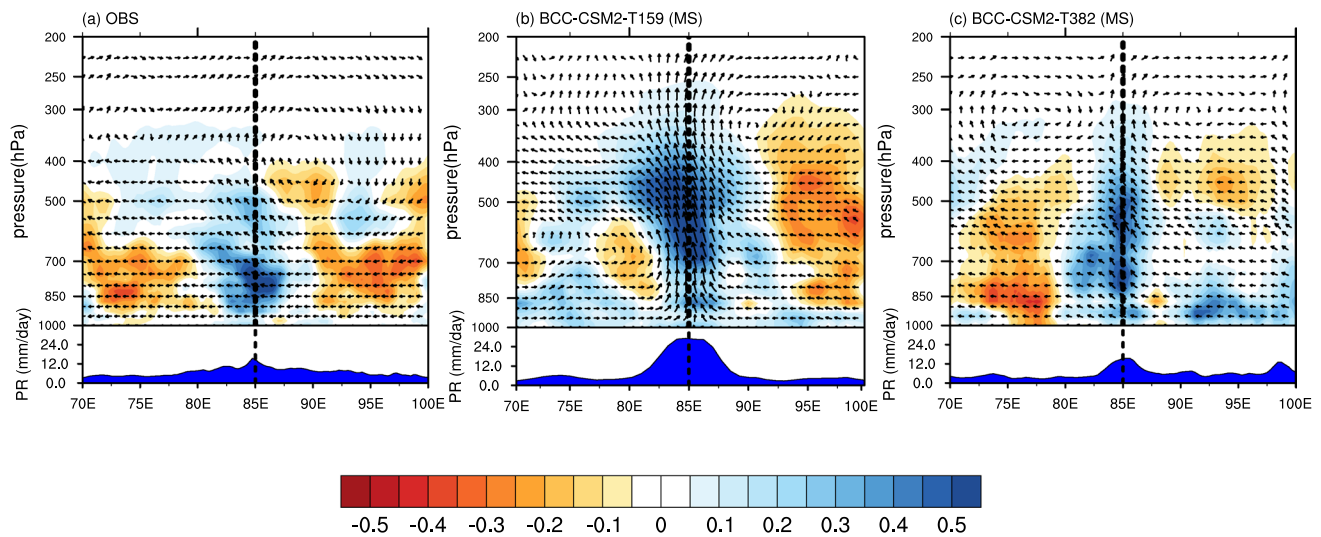
Fig. 18 Longitude–height cross–sections of composite specific humidity tendency (shading, unit: g kg^{-1} day^{-1}) overlaid with wind vectors (u, w) and the longitudinal distribution of the composite precipitation (unit: mm day^{-1}) for multiple strong MJO events propagating eastward to 85° E averaged over 10° N–10° S for **a** ERA5, **b** BCC-CSM2-T159 (MS) and **c** BCC-CSM2-T382 (MS). The vertical dashed line represents the position of the convective center at 85° E averaged over 10° N–10° S

performances of MJO simulation in BCC-CSM2 models are superior to those in BCC-AGCM3 models, indicating that atmosphere–ocean interactions are important for MJO simulations in BCC models.

This study also reveals that the high-resolution model (BCC-CSM2-T382) has stronger MJO spectra, longer periods, higher explained variance, and stronger MJO signals than the medium-resolution model (BCC-CSM2-T159), but with overestimation in most features. This indicates that increasing the model resolution alone may not improve the simulation capability of the MJO.

We investigate the physical mechanism for the improvements in the simulation of the MJO by analyzing the moisture and atmospheric circulation related to the MJO in the MS experiments. The MS experiments of both BCC-CSM2-T159 and BCC-CSM2-T382 capture the structures of water vapor and vertical circulation circle near the MJO convection center similar to the observations. The transport processes enhance moisture exchange from the lower troposphere to the upper troposphere around convective clouds, and promote the convergence of moisture in the lower troposphere to the east of the convection center, and then induce eastward propagation of the MJO.

Our analyses show that both BCC-CSM2-T159 and BCC-CSM2-T382 still have some biases in the strength, structure and propagation of the MJO simulations. For example, BCC-CSM2-T382 with the modified deep convection scheme has no evident improvement in the simulation of the spatial structure of CEOFs than that with the original scheme. The modified deep convection scheme exerts less influence on the structure of the MJO in BCC-CSM2-T382 than that in

BCC-CSM2-T159. Further improvements are needed in the future. In our future study, we will initialize the two models to predict a typical MJO event in both OS experiments and MS experiments. This will provide evidence for improving the MJO prediction skill. Whether the modified deep convection scheme has benefits for Quasi–biennial Oscillation (QBO) simulations, as QBO is strongly linked to MJO events, will be investigated in our future work.

2018). The model output data generated during the current study are not publicly available but are available from the corresponding author on reasonable request.

Declarations

Conflict of interest The authors declare no conflicts of interest relevant to this study.

Open Access This article is licensed under a Creative Commons Attribution 4.0 International License, which permits use, sharing, adaptation, distribution and reproduction in any medium or format, as long as you give appropriate credit to the original author(s) and the source, provide a link to the Creative Commons licence, and indicate if changes were made. The images or other third party material in this article are included in the article's Creative Commons licence, unless indicated otherwise in a credit line to the material. If material is not included in the article's Creative Commons licence and your intended use is not permitted by statutory regulation or exceeds the permitted use, you will need to obtain permission directly from the copyright holder. To view a copy of this licence, visit http://creativecommons.org/licenses/by/4.0/.

References

Adler R, Wang JJ, Sapiano M, Huffman G, Bolvin D, Nelkin E and NOAA CDR Program (2017) Global Precipitation Climatology Project (GPCP) Climate Data Record (CDR), Version 1.3 (Daily) [Indicate subset used.]. NOAA National Centers for Environmental Information. https://doi.org/10.7289/V5RX998Z

Ahn MS, Kim D, Sperber KR et al (2017) MJO simulation in CMIP5 climate models: MJO skill metrics and process-oriented diagnosis. Clim Dyn 49:4023–4045. https://doi.org/10.1007/s00382-017-3558-4

Ahn MS, Kim D, Park S et al (2019) Do we need to parameterize mesoscale convective organization to mitigate the MJO-mean state trade-off? Geophys Res Lett 46:2293–2301. https://doi.org/10.1029/2018GL080314

Akhila RS, Kuttippurath J, Rahul R et al (2022) Genesis and simultaneous occurrences of the super cyclone Kyarr and extremely severe cyclone Maha in the Arabian Sea in October 2019. Nat Hazards 113:1133–1150. https://doi.org/10.1007/s11069-022-05340-9

Baggett CF, Nardi KM, Childs SJ et al (2018) Skillful subseasonal forecasts of weekly tornado and hail activity using the Madden-Julian Oscillation. J Geophys Res Atmos 123:12661–12675. https://doi.org/10.1029/2018JD029059

Bartana H, Garfinkel CI, Shamir O et al (2023) Projected future changes in equatorial wave spectrum in CMIP6. Clim Dyn 60:3277–3289. https://doi.org/10.1007/s00382-022-06510-y

Bechtold P, Köhler M, Jung T et al (2008) Advances in simulating atmospheric variability with the ECMWF model: From synoptic to decadal time-scales. Q J R Meteorol Soc 134:1337–1351. https://doi.org/10.1002/qj.289

Cao G, Zhang GJ (2017) Role of vertical structure of convective heating in MJO simulation in NCAR CAM5.3. J Clim 30:7423–7439. https://doi.org/10.1175/JCLI-D-16-0913.1

Chen X, Zhang F (2019) Relative roles of preconditioning moistening and global circumnavigating mode on the MJO convective initiation during DYNAMO. Geophys Res Let 46:1079–1087. https://doi.org/10.1029/2018GL080987

Chen G, Ling J, Zhang R et al (2022) The MJO from CMIP5 to CMIP6: Perspectives from tracking MJO precipitation. Geophys Res Lett 49:e2021GL095241. https://doi.org/10.1029/2021GL095241

Crueger T, Stevens B, Brokopf R (2013) The Madden–Julian oscillation in ECHAM6 and the introduction of an objective MJO metric. J Clim 26:3241–3257. https://doi.org/10.1175/JCLI-D-12-00413.1

Del Genio AD, Wu J, Wolf AB et al (2015) Constraints on cumulus parameterization from simulations of observed MJO events. J Clim 28:6419–6442. https://doi.org/10.1175/JCLI-D-14-00832.1

Deng L, Wu X (2010) Effects of convective processes on GCM simulations of the Madden–Julian oscillation. J Clim 23:352–377. https://doi.org/10.1175/2009JCLI3114.1

Deng Q, Khouider B, Majda AJ (2015) The MJO in a coarse-resolution GCM with a stochastic multicloud parameterization. J Atmos Sci 72:55–74. https://doi.org/10.1175/JAS-D-14-0120.1

Duvel JP, Bellenger H, Bellon G, Remaud M (2013) An event-by-event assessment of tropical intraseasonal perturbations for general circulation models. Clim Dyn 40:857–873. https://doi.org/10.1007/s00382-012-1303-6

Eyring V, Bony S, Meehl GA et al (2016) Overview of the Coupled Model Intercomparison Project Phase 6 (CMIP6) experimental design and organization. Geosci Model Dev 9:1937–1958. https://doi.org/10.5194/gmd-9-1937-2016

Feng X, Yang GY, Hodges KI et al (2023) Equatorial waves as useful precursors to tropical cyclone occurrence and intensification. Nat Commun 14:511. https://doi.org/10.1038/s41467-023-36055-5

Goswami BB, Khouider B, Phani R et al (2017) Improving synoptic and intraseasonal variability in CFSv2 via stochastic representation of organized convection. Geophys Res Lett 44:1104–1113. https://doi.org/10.1002/2016GL071542

Hannah WM, Maloney ED (2011) The role of moisture–convection feedbacks in simulating the Madden–Julian oscillation. J Clim 24:2754–2770. https://doi.org/10.1175/2011JCLI3803.1

Hannah WM, Maloney ED, Pritchard MS (2015) Consequences of systematic model drift in DYNAMO MJO hindcasts with SP-CAM and CAM5. J Adv Model Earth Syst 7:1051–1074. https://doi.org/10.1002/2014MS000423

Hersbach H, Bell B, Berrisford P et al (2018) ERA5 hourly data on single levels from 1979 to present. In: Copernicus climate change service (c3s) climate data store (cds) 10(10.24381).

Hung MP, Lin JL, Wang W et al (2013) MJO and convectively coupled equatorial waves simulated by CMIP5 climate models. J Clim 26:6185–6214. https://doi.org/10.1175/JCLI-D-12-00541.1

Jia X, Li C, Ling J et al (2008) Impacts of a GCM's resolution on MJO simulation. Adv Atmos Sci 25:139–156. https://doi.org/10.1007/s00376-008-0139-9

Jiang X, Waliser DE, Xavier PK et al (2015) Vertical structure and physical processes of the Madden-Julian oscillation: Exploring key model physics in climate simulations. J Geophys Res Atmos 120:4718–4748. https://doi.org/10.1002/2014JD022375

Khairoutdinov M, Randall D, DeMott C (2005) Simulations of the atmospheric general circulation using a cloud-resolving model as a superparameterization of physical processes. J Atmos Sci 62:2136–2154. https://doi.org/10.1175/JAS3453.1

Kim D, Maloney ED (2017) Simulation of the Madden-Julian oscillation using general circulation models. In: The global monsoon system: research and forecast, pp 119–130. https://doi.org/10.1142/9789813200913_0009

Klotzbach PJ, Oliver ECJ (2015) Modulation of Atlantic basin tropical cyclone activity by the Madden–Julian oscillation (MJO) from 1905 to 2011. J Clim 28:204–217. https://doi.org/10.1175/JCLI-D-14-00509.1

Klotzbach PJ, Schreck CJ III, Compo GP et al (2023) Influence of the Madden-Julian oscillation on continental United States Hurricane Landfalls. Geophys Res Let 50:e2023GL102762. https://doi.org/10.1029/2023GL102762

Landu K, Maloney ED (2011) Effect of SST distribution and radiative feedbacks on the simulation of intraseasonal variability in an

aquaplanet GCM. J Meteorol Soc Jap 89:195–210. https://doi.org/10.2151/jmsj.2011-302

Latos B, Peyrillé P, Lefort T et al (2023) The role of tropical waves in the genesis of Tropical Cyclone Seroja in the Maritime Continent. Nat Commun 14:856. https://doi.org/10.1038/s41467-023-36498-w

Lau WKM, Waliser DE (2011) Intraseasonal variability in the atmosphere-ocean climate system. Springer Science & Business Media. https://doi.org/10.1007/978-3-642-13914-7

Lenka S, Gouda KC, Devi R et al (2023) Dynamical influence of MJO phases on the onset of Indian Monsoon. Environ Res Commun. https://doi.org/10.1088/2515-7620/acde3a

Li T, Zhao C, Hsu PC, Nasuno T (2015) MJO initiation processes over the tropical Indian Ocean during DYNAMO/CINDY2011. J Clim 28:2121–2135. https://doi.org/10.1175/JCLI-D-14-00328.1

Li X, Tang Y, Zhou L et al (2016) Assessment of Madden–Julian oscillation simulations with various configurations of CESM. Clim Dyn 47:2667–2690. https://doi.org/10.1007/s00382-016-2991-0

Li J, Yang Y, Zhu Z (2020) Application of MJO dynamics-oriented diagnostics to CMIP5 models. Theoret Appl Climatol 141:673–684. https://doi.org/10.1007/s00704-020-03185-5

Li Y, Wu J, Luo JJ et al (2022) Evaluating the Eastward propagation of the MJO in CMIP5 and CMIP6 models based on a variety of diagnostics. J Clim 35:1719–1743. https://doi.org/10.1175/JCLI-D-21-0378.1

Liang Y, Fedorov AV (2021) Linking the Madden–Julian Oscillation, tropical cyclones and westerly wind bursts as part of El Niño development. Clim Dyn 57:1039–1060. https://doi.org/10.1007/s00382-021-05757-1

Liebmann B, Smith CA (1996) Description of a complete (interpolated) outgoing longwave radiation dataset. Bull Am Meteor Soc 77:1275–1277

Lin JL, Kiladis GN, Mapes BE et al (2006) Tropical intraseasonal variability in 14 IPCC AR4 climate models. Part i: convective signals. J Clim 19:2665–2690. https://doi.org/10.1175/JCLI3735.1

Lin JL, Lee MI, Kim D, Kang IS, Frierson DM (2008) The impacts of convective parameterization and moisture triggering on AGCM-simulated convectively coupled equatorial waves. J Clim 21:883–909. https://doi.org/10.1175/2007JCLI1790.1

Ling J, Li C (2014) Impact of convective momentum transport by deep convection on simulation of tropical intraseasonal oscillation. J Ocean Univ China 13:717–727. https://doi.org/10.1007/s11802-014-2295-0

Liu X, Li W, Wu T et al (2019) Validity of parameter optimization in improving MJO simulation and prediction using the sub-seasonal to seasonal forecast model of Beijing Climate Center. Clim Dyn 52:3823–3843. https://doi.org/10.1007/s00382-018-4369-y

Liu Y, Tan ZM, Wu Z (2022) Enhanced feedback between shallow convection and low-level moisture convergence leads to improved simulation of MJO eastward propagation. J Clim 35:591–615. https://doi.org/10.1175/JCLI-D-20-0894.1

Loeb NG, Doelling DR, Wang H et al (2018) Clouds and the earth's radiant energy system (CERES) energy balanced and filled (EBAF) top-of-atmosphere (TOA) edition-4.0 data product. J Clim 31:895–918. https://doi.org/10.1175/JCLI-D-17-0208.1

Madden RA, Julian PR (1971) Detection of a 40–50 day oscillation in the zonal wind in the tropical Pacific. J Atmos Sci 28:702–708. (**10.1175/1520-0469(1971)028<0702:DOADOI>2.0.CO;2**)

Madden RA, Julian PR (1972) Description of global-scale circulation cells in the tropics with a 40–50 day period. J Atmos Sci 29:1109–1123. https://doi.org/10.1175/1520-0469(1972)029%3c1109:DOGSCC%3e2.0.CO;2

Maloney ED, Hartmann DL (2001) The sensitivity of intraseasonal variability in the NCAR CCM3 to changes in convective parameterization. J Clim 14:2015–2034. https://doi.org/10.1175/1520-0442(2001)014%3c2015:TSOIVI%3e2.0.CO;2

Malviya S, Mukhopadhyay P, Phani Murali Krishna R et al (2018) Mean and intra-seasonal variability simulated by NCEP Climate Forecast System model (version 2.0) during boreal winter: Impact of horizontal resolution. Int J Climatol 38:3028–3043. https://doi.org/10.1002/joc.5480

Meehl GA, Covey C, Delworth T et al (2007) The WCRP CMIP3 multimodel dataset: a new era in climate change research. Bull Am Meteorol Soc 88:1383–1394. https://doi.org/10.1175/BAMS-88-9-1383

Miller DE, Gensini VA, Barrett BS (2022) Madden-Julian oscillation influences United States springtime tornado and hail frequency. Npj Clim Atmos Sci 5:37. https://doi.org/10.1038/s41612-022-00263-5

Newman M, Sardeshmukh PD, Penland C (2009) How important is air–sea coupling in ENSO and MJO evolution. J Clim 22:2958–2977. https://doi.org/10.1175/2008JCLI2659.1

Pathak R, Sahany S, Mishra SK (2021) Impact of stochastic entrainment in the NCAR CAM deep convection parameterization on the simulation of South Asian Summer Monsoon. Clim Dyn 57:3365–3384. https://doi.org/10.1007/s00382-021-05870-1

Pegion K, Kirtman BP (2008) The impact of air–sea Interactions on the simulation of tropical intraseasonal variability. J Clim 21:6616–6635. https://doi.org/10.1175/2008JCLI2180.1

Rajendran K, Kitoh A, Mizuta R et al (2008) High-resolution simulation of mean convection and its intraseasonal variability over the tropics in the MRI/JMA 20-km mesh AGCM. J Clim 21:3722–3739. https://doi.org/10.1175/2008JCLI1950.1

Roxy MK, Dasgupta P, McPhaden MJ et al (2019) Twofold expansion of the Indo-Pacific warm pool warps the MJO life cycle. Nature 575:647–651. https://doi.org/10.1038/s41586-019-1764-4

Savarin A, Chen SS (2022) Pathways to better prediction of the MJO: 1. Effects of model resolution and moist physics on atmospheric boundary layer and precipitation. J Adv Model Earth Syst 14:e2021MS002928. https://doi.org/10.1029/2021MS002928

Seo KH, Wang W (2010) The Madden–Julian oscillation simulated in the NCEP Climate Forecast System model: The importance of stratiform heating. J Clim 23:4770–4793. https://doi.org/10.1175/2010JCLI2983.1

Slingo JM, Sperber KR, Boyle JS et al (1996) Intraseasonal Oscillations in 15 atmospheric general circulation models: Results from an AMIP diagnostic subproject. Clim Dyn 12:325–357. https://doi.org/10.1007/BF00231106

Sperber KR, Gualdi S, Legutke S et al (2005) The Madden–Julian oscillation in ECHAM4 coupled and uncoupled general circulation models. Clim Dyn 25:117–140. https://doi.org/10.1007/s00382-005-0026-3

Stephens GL, Li J, Wild M et al (2012) An update on Earth's energy balance in light of the latest global observations. Nat Geosci 5:691–696. https://doi.org/10.1038/ngeo1580

Taylor KE, Stouffer RJ, Meehl GA (2012) An overview of CMIP5 and the experiment design. Bull Am Meteorol Soc 93:485–498. https://doi.org/10.1175/BAMS-D-11-00094.1

Tokioka T, Yamazaki K, Kitoh A, Ose T (1988) The equatorial 30–60 day oscillation and the Arakawa-Schubert penetrative cumulus parameterization. J Meteorol Soc Jpn Ser II 66:883–901. https://doi.org/10.2151/jmsj1965.66.6_883

Tseng WL, Hsu HH, Lan YY et al (2022) Improving Madden–Julian oscillation simulation in atmospheric general circulation models by coupling with a one-dimensional snow–ice–thermocline ocean model. Geosci Model Dev 15:5529–5546. https://doi.org/10.5194/gmd-15-5529-2022

Vitart F (2009) Impact of the Madden Julian Oscillation on tropical storms and risk of landfall in the ECMWF forecast system. Geophys Res Lett. https://doi.org/10.1029/2009GL039089

Springer

Vitart F, Molteni F (2010) Simulation of the Madden–Julian oscillation and its teleconnections in the ECMWF forecast system. Q J R Meteorol Soc 136:842–855. https://doi.org/10.1002/qj.623

Vitart F, Ardilouze C, Bonet A et al (2017) The subseasonal to seasonal (S2S) prediction project database. Bull Am Meteorol Soc 98:163–173. https://doi.org/10.1175/BAMS-D-16-0017.1

Waliser D, Sperber K, Hendon H et al (2009) MJO simulation diagnostics. J Clim 22:3006–3030. https://doi.org/10.1175/2008JCLI2731.1

Wang B, Lee SS (2017) MJO propagation shaped by zonal asymmetric structures: results from 24 GCM simulations. J Clim 30:7933–7952. https://doi.org/10.1175/JCLI-D-16-0873.1

Wang W, Schlesinger ME (1999) The dependence on convection parameterization of the tropical intraseasonal oscillation simulated by the UIUC 11-layer atmospheric GCM. J Clim 12:1423–1457. https://doi.org/10.1175/1520-0442(1999)012%3c1423:TDOCPO%3e2.0.CO;2

Wang Z, Boyd K, Walsh JE (2023) Modulation of polar low activity by the Madden-Julian oscillation. Geophys Res Let 50:e2023GL103719. https://doi.org/10.1029/2023GL103719

Wheeler MC, Hendon HH (2004) An all-season real-time multivariate MJO index: Development of an index for monitoring and prediction. Mon Weather Rev 132:1917–1932. https://doi.org/10.1175/1520-0493(2004)132%3c1917:AARMMI%3e2.0.CO;2

Wheeler MC, Hendon HH, Cleland S, Meinke H, Donald A (2009) Impacts of the Madden–Julian oscillation on Australian rainfall and circulation. J Clim 22:1482–1498. https://doi.org/10.1175/2008JCLI2595.1

Wild M (2020) The global energy balance as represented in CMIP6 climate models. Clim Dyn 55:553–577. https://doi.org/10.1007/s00382-020-05282-7

Wu T (2012) A mass-flux cumulus parameterization scheme for large-scale models: description and test with observations. Clim Dyn 38:725–744. https://doi.org/10.1007/s00382-011-0995-3

Wu T, Li W, Ji J et al (2013) Global carbon budgets simulated by the Beijing Climate Center Climate System Model for the last century. J Geophys Res Atmos 118:4326–4347. https://doi.org/10.1002/jgrd.50320

Wu T, Song L, Li W et al (2014) An overview of BCC climate system model development and application for climate change studies. J Meteorol Res 28:34–56. https://doi.org/10.1007/s13351-014-3041-7

Wu T, Lu Y, Fang Y et al (2019) The Beijing Climate Center Climate System Model (BCC-CSM): the main progress from CMIP5 to CMIP6. Geosci Model Dev 12:1573–1600. https://doi.org/10.5194/gmd-12-1573-2019

Wu T, Yu R, Lu Y et al (2021) BCC-CSM2-HR: a high-resolution version of the Beijing Climate Center Climate System Model. Geosci Model Dev 14:2977–3006. https://doi.org/10.5194/gmd-14-2977-2021

Xin X, Zhang L, Zhang J (2013) Climate change projections over East Asia with BCC_CSM1. 1 climate model under RCP scenarios. J Meteorol Soc Jpn Ser II 91:413–429. https://doi.org/10.2151/jmsj.2013-401

Zaitchik BF (2017) Madden-Julian Oscillation impacts on tropical African precipitation. Atmos Res 184:88–102. https://doi.org/10.1016/j.atmosres.2016.10.002

Zhang C (2005) Madden-julian oscillation. Rev Geophys. https://doi.org/10.1029/2004RG000158

Zhang C (2013) Madden–Julian oscillation: Bridging weather and climate. Bull Am Meteorol Soc 94:1849–1870. https://doi.org/10.1175/BAMS-D-12-00026.1

Zhang C, Hendon HH (1997) Propagating and standing components of the intraseasonal oscillation in tropical convection. J Atmos Sci 54:741–752. https://doi.org/10.1175/1520-0469(1997)054%3c0741:PASCOT%3e2.0.CO;2

Zhang GJ, Mu M (2005) Simulation of the Madden–Julian oscillation in the NCAR CCM3 using a revised Zhang–McFarlane convection parameterization scheme. J Clim 18:4046–4064. https://doi.org/10.1175/JCLI3508.1

Zhao N, Nasuno T (2020) How does the air-sea coupling frequency affect convection during the Mjo passage? J Adv Model Earth Syst 12:e2020MS002058. https://doi.org/10.1029/2020MS002058

Zheng C, Kar-Man Chang E, Kim HM, Zhang M, Wang W (2018) Impacts of the Madden–Julian oscillation on storm-track activity, surface air temperature, and precipitation over North America. J Clim 31:6113–6134. https://doi.org/10.1175/JCLI-D-17-0534.1